Geochemistry, Geophysics, Geosystems®

Combined Genomic and Imaging Techniques Show Intense Arsenic Enrichment Caused by Detoxification in a Microbial Mat of the Dead Sea Shore

C. Thomas[1,2] , M. Filella[3] , D. Ionescu[4], S. Sorieul[5], C. G. L. Pollier[6] , A. M. Oehlert[6], P. Zahajská[7,8] , N. Gedulter[9], A. Agnon[9] , D. Ferreira Sanchez[10], and D. Ariztegui[1]

[1]Department of Earth Sciences, University of Geneva, Geneva, Switzerland, [2]Now at Institute of Geological Sciences and Oeschger Centre for Climate Research, University of Bern, Bern, Switzerland, [3]Department F.-A. Forel, University of Geneva, Geneva, Switzerland, [4]Leibniz Institute for Freshwater Ecology and Inland Fisheries, Stechlin, Germany, [5]CNRS, University of Bordeaux, LP2iB, Gradignan, France, [6]Rosenstiel School of Marine, Atmospheric, and Earth Science, University of Miami, Miami, FL, USA, [7]Institute of Geography & Oeschger Centre for Climate Change Research, University of Bern, Bern, Switzerland, [8]Institute of Geology and Palaeontology, Faculty of Science, Charles University, Prag, Czechia, [9]Institute of Earth Sciences, Hebrew University of Jerusalem, Jerusalem, Israel, [10]Swiss Light Source, Paul Scherrer Institute, Villigen, Switzerland

Abstract Microbial mats and microbialites are essential tools for reconstructing early life and its environments. To better understand microbial trace element cycling, a microbial mat was collected from the sinkhole systems of the western shores of the Dead Sea, a dynamic environment exhibiting diverse extreme environments. Intense arsenic enrichment was measured (up to 6.5 million times higher than current concentrations in water, and 400 times the bulk concentration in the mat). Arsenic was found predominantly as As(V) in organic molecules, as shown by XANES spectra and high-resolution elemental mapping. Arsenic cycling genes obtained from metagenomic analysis were associated with arsenic detoxification, supporting an active mechanism of As(V) uptake, As(III) efflux and organoarsenic accumulation in the extracellular polymeric substances (EPS) of the mat. Thus, we propose that such localized As enrichment can be attributed to a transient increase in As(V) concentrations in the circulating subsurface water of the Dead Sea shore and its subsequent incorporation into organoarsenic molecules through microbial detoxification processes. Our data set supports the possibility of metalloid enrichment recorded in very localized facies due to rapid geogenic fluctuations in the chemistry of the water flowing over a biofilm. In this context, this example calls for caution in interpreting metal(loid) enrichment in organic matter-rich layers and microbialites of Paleoproterozoic origin. Arsenic signatures in Precambrian organic matter and carbonate rocks may host biosignatures, including evidence for extracellular polymeric substances, As-binding and detoxification processes, without supporting arsenotrophy. However, they provide clues to better assess the paleoenvironmental conditions at the time of microbial mat formation.

Plain Language Summary Microbial mats and microbialites are like time machines helping us learn about ancient life and its environments. We collected a microbial mat from the unique Dead Sea's sinkholes, where life thrives in extreme conditions. In this mat, we found for the first time in this area a staggering 6.5 million-fold increase in arsenic, an element toxic to life. By closely studying the genes and chemistry of this microbial mat, we discovered that microbes were striving to clean up this excess arsenic in a sort of natural detoxification process. It seems that a temporary spike in arsenic levels in the Dead Sea water triggered this clean-up work, which eventually stored the arsenic safely in the mat away from the microbial cells. Our findings suggest that in the past, when microbial mats were one of the only ecosystems on Earth, changes in the water flowing over mats like this one could have caused similar accumulations of metals. Therefore, when scientists study ancient fossilized microbial layers, these discoveries can help us look into the past and understand the chemical and biological conditions under which these ancient microbial mats formed.

1. Introduction

Despite its low abundance in the Earth's crust, arsenic (As) is a common element in the environment. It is known for its toxicity to life mainly because of the use of As_2O_3 for murders by poisoning. What is true for humans is also true for the rest of the tree of life. For example, the common form of As in the environment, arsenate -As(V)-, is

Validation: M. Filella, D. Ionescu, A. M. Oehlert, A. Agnon, D. Ferreira Sanchez, D. Ariztegui
Writing – original draft: C. Thomas
Writing – review & editing: C. Thomas, M. Filella, D. Ionescu, S. Sorieul, C. G. L. Pollier, A. M. Oehlert, P. Zahajská, N. Gedulter, A. Agnon, D. Ferreira Sanchez, D. Ariztegui

molecularly close to phosphate and can enter microbial cells via phosphate transporters and inhibit oxidative phosphorylation. Several mechanisms have evolved to cope with and remove As from cells. They generally involve arsenate -As(V)- reduction to arsenite -As(III)- and expulsion pathways through the *Ars* operon, involving the transport of arsenite and/or methylation reactions into fewer and non-toxic organic molecules (Rosen, 2002; Xu et al., 1998). Some examples found in the environment are methylarsonate, dimethylarsinate, mono and dimethylarsinic acid, trimethylarsine oxide, tetramethylarsonium or volatile trimethylarsine (Honschopp et al., 1996; Lakso & Peoples, 1975; Mcbride & Wolfe, 1971; Zhu et al., 2014), arsenobetaine (the only non-toxic organoarsenic; Caumette et al., 2012; Edmonds et al., 1977), or arseno-sugars (Morita & Shibata, 1990). In this context, life plays an important role in global As cycling through the employment of such detoxification processes. Additionally, some prokaryotes also use As(V) as their respiratory oxidant coupled to organic matter oxidation (Oremland & Stolz, 2003). These dissimilatory arsenate-reducing organisms include *Proteobacteria*, *Firmicutes*, *Clostridia*, and thermophilic *Archaea* isolated from freshwater sediments, soda lakes, hot springs (Oremland & Stolz, 2003), aquifers (Saikat et al., 2001) or animal digestive tracts (Herbel et al., 2002). They all use an arsenate respiratory reductase (*arr*) thought to have evolved from the polysulfide reductase enzyme allowing respiratory conversion of S^0 to H_2S (Duval et al., 2008). Heterotrophic and chemolithoautotrophic arsenite oxidizers can also cycle arsenite as a detoxification system using the *aio* enzyme (Anderson et al., 1992) or through the use of As(III) as electron donor for nitrate reduction (Zargar et al., 2010) or anoxygenic photosynthesis (Kulp et al., 2008) via the *arxA* gene found in *Gammaproteobacteria Thioalkalivibrio* and *Halomonas* for example, (Edwardson & Hollibaugh, 2017). *ArxA*, *aioA*, *arrA* all belong to the Dimethylsulfoxide (DMSO) reductase superfamily of molybdenum-containing enzymes (Andres & Bertin, 2016; McEwan et al., 2002). Arsenite oxidase (*aio*) has been suggested to emerge before the Archaea/Bacteria divide (Lebrun et al., 2003), inferring the presence and role of arsenite in biogeochemical cycling of Archean habitats (Mukhopadhyay et al., 2002; Sforna et al., 2014), along with mechanisms to cope with its toxicity (Chen et al., 2020). Respiratory arsenate reductase (*arrA*), and the arsenate resistance system is suggested to have evolved contemporaneously with the oxygenation of the atmosphere (Duval et al., 2008), in concert with increased photosynthetic activity around the Great Oxidation Event (Chen et al., 2020), although debate exists for Archean antiquity of *arrA* (Kulp et al., 2008; Schoepp-Cothenet et al., 2009). Arsenic has therefore become an element of prime interest for geobiology studies as it may hint at early Earth microbial cycling.

Analogous environments in modern settings where active As cycling has been identified have been used to better assess the potential of As-based ecosystems. Numerous studies of the hypersaline and alkaline environments of the high-altitude Andean lakes (Farías et al., 2013; Fernandez et al., 2016; Sancho-Tomás et al., 2018; Saona et al., 2021), Searles Lake (Oremland et al., 2005) and Mono Lake (Kulp et al., 2008; Switzer et al., 1998) have advanced our understanding of As cycling. Some of these environments contain microbial mats that can be seen as modern equivalents of primordial ecosystems exhibiting As cycling (Visscher et al., 2020). These modern examples could explain As enrichment in fossilized microbial structures observed for the Archean Dresser Formation stromatolites (Baumgartner et al., 2020) and the Tumbiana stromatolites (Sforna et al., 2014), where the coupling of As cycling with anoxygenic photosynthesis has been hypothesized to be a potential phototrophic pathway before the emergence of oxygenic photosynthesis (Oremland et al., 2009).

In the Dead Sea water, potentially toxic trace element concentrations are relatively high (Nissenbaum, 1977), but their levels are not considered to be "seriously limiting to life" (Oren, 1983). Adaptations to these elevated concentrations have nonetheless been identified in DNA extracted from subsurface evaporitic units (Thomas et al., 2014). In contrast, As is neither enriched in the brines nor in the mud of the modern Dead Sea. Kotova et al. (2016) measured As concentrations of 0.01 mg.L^{-1} in the Dead Sea Brine, and up to 3 mg.L^{-1} in shallow Dead Sea mud of the western shore. Similar ranges of concentrations were measured from the eastern shore mud (Abdel-Fattah & Pingitore, 2009).

Metalloid-like use by microbes from the Dead Sea was identified in a selenate-breathing anaerobic bacterium isolated from shallow sediments (Switzer et al., 2001). High metabolic diversity was found in microbial mats near and within underwater freshwater springs (Ionescu et al., 2012), including phototrophic communities (green and purple sulfur bacteria, cyanobacteria) and potential metal reducers (mainly associated with Fe-cycling). While life in the Dead Sea brines is strongly limited by hypersalinity and high divalent cation concentrations (Oren, 1999, 2010), dilution of the brine by freshwater spring onshore (Adar et al., 2014; Hirshberg & Ben-Ami, 2019) or offshore (Häusler, Noriega-Ortega, et al., 2014; Ionescu et al., 2012), or by heavy rainfalls (Levy et al., 2022;

Oren, 1993; Oren et al., 1995), allows the diversification of microbial communities and metabolic potential, including the possible use of other metalloids.

The Dead Sea lake level has been dropping by ca. 1 m per year for the last 30 years (Abu Ghazleh et al., 2009; Lensky et al., 2005). Freshwater aquifers follow the retreat of the denser Dead Sea Brine as lake level drops and infiltrate the Quaternary lacustrine deposits of the Dead Sea paleolake (Shalev et al., 2006; Yechieli et al., 2006). Inside these evaporitic formations, halite is easily dissolved by the circulating subsurface freshwater, which leads to land instability, epitomized by frameworks of fractures and sinkhole formation along the coasts of the Dead Sea (Closson & Abou Karaki, 2009; Nof et al., 2019). Some circulating freshwater may emerge and form springs of varying chemistry, heat, and salinity depending on their hydrographic specificity (interactions with groundwater, brine, sediments…). The resulting structures are often networks of ponds and sinkholes providing favorable conditions for the development of diverse life (Hirshberg & Ben-Ami, 2019), including microbial communities and microbial mats (Adar et al., 2014; Ionescu et al., 2012; Thomas et al., 2021).

We identified As-rich environments and associated microbial mats in the sinkhole systems of Dead Sea western shores. Here, we investigate this actively accreting microbialite environment to determine whether it has the potential to serve as a model system for As biosignature incorporation in living microbial mats, providing needed insight into fossilized counterparts. In this study, we use a combination of imaging techniques (including fluorescent/hyperspectral microscopy), (meta)genomics, mass spectrometry, and synchrotron-based techniques to map the elemental distribution and microbial structure of the As-rich microbial mat. Together, these analyses allow us to assess the characteristics of As and its relationship to intact in situ biological features. Our objective is to better understand the processes leading to the incorporation of As and trace metal (bio)signatures into microbial mats potentially recognizable as analogs of Precambrian ecosystems and ancient microbial stratiform deposits.

2. Materials and Methods

2.1. Sampling Site

The investigated sinkhole is located at 31.4744°N and 35.3987°E, close to the Ein Gedi Kibbutz (Figure 1a). It lies within a small system of recently formed sinkholes (named "pools" in Figures 1b and 1c) exhibiting biofilms and microbial mats of different colors and textures. At the time of sampling (January 2020), the sinkhole of interest (pool 1 in Figure 1c) was a 2 m in diameter and 40 cm deep depression at its maximum, situated at an altitude of −431.6 m above sea level (Figures 1c and 1d). It was the highest pool of the whole system, it was among the coldest ones (Pool 1, 22.9°C) and had the lowest salinity (27.9 g.L^{-1} TDS). No water source or outflow could be located in pool 1. However, the water temperature rose right at the base of the Dead Sea-facing exterior rim of pool 1, where we located an outflow of water (active hot spring) with temperatures reaching 30°C (marked by an arrow in Figure 1c). This water fed a stream flowing into a series of interconnected ponds downstream (from pool 2 to pool 7) almost all the way to the Dead Sea (temperature and pH measured for the Dead Sea: $T = 24.5$°C, pH = 6, 5). The bottom of pool 1 was draped by a partly mineralized microbial mat of ca. 2–4 cm thickness, immersed in water with an Eh of 26.6 mV and a pH of 7.8. The surface of the mat was pustular with brownish to orange mineral clusters ($CaCO_3$) intertwined at its base by green wavy gel-like laminae on top of a pink wavy lamina. A dark brown to dark gray biofilm layer formed the base of the mat (Figure 1e).

2.2. Field Sampling and Sample Preparation

Microbial mats, water samples, and in situ measurements of environmental parameters were collected in January 2020. Fresh sections of the microbial mat were collected in plastic boxes and kept immersed in the pool water. The microbial mat section used for pigment and elemental imaging was subsampled on site and kept cool (4°C) in a plastic vial until resin embedding in the geomicrobiology laboratory of the Earth Science Department at the University of Geneva a few days after sampling. There, the 1.5 cm long sample was immersed in successive baths of absolute ethanol (99% purity), and then in freshly opened acrylic LR white resin (Sigma Aldrich®, Merck KGaA, Darmstadt, Germany). The sample was brought to 40°C for 1 hr and further incubated at 60°C for 3 days to achieve maximum desiccation. The resulting LR white resin-embedded microbial mat was then engulfed in classic epoxy resin Epo-Tek® 301 (Epoxy Technology, inc., Billerica, MA, USA) and mirror polished.

Figure 1. Photographs of sampling system and location. The location of the sinkhole system (white dot) on the western shore of the Dead Sea within the Levantine region (a). A network of several ponds formed by evaporite dissolution by circulating fresh water flowing toward the Dead Sea was sampled. Samples and data presented originate from the pool identified by the black arrow (b), named pool 1 in the drone photo showing the sinkhole system and its overall properties (c). Zoomed-in photo of pool 1 (d), and field photo of the well-laminated microbial mat (e). Water circulates from pool 2 to pool 7. However, no water was clearly observed flowing out of pool 1 and pool 1b suggesting a disconnection of these two pools, with a spring slightly above pool 2 feeding pools 2 to pool 7.

2.3. Epifluorescence Microscopy

The resin-embedded sample was used to observe natural autofluorescence using a LSM780 Airyscan Zeiss microscope and filters adapted to DAPI (excitation wavelength 353 nm, emission wavelength 465 and detection between 400 and 509 nm), APC (excitation wavelength 651 nm, emission wavelength 660 nm and detection between 635 and 700 nm) and Rhodamine (excitation wavelength 558 nm, emission wavelength 575 nm and detection between 562 and 700 nm), and processed using the Zen 3.2 imaging software by Carl Zeiss Microscopy GmbH© (Oberkochen, Germany), at the Bioimaging Center of the University of Geneva.

2.4. Elemental Chemistry of the Pool Water and Bulk Microbial Mat

Water parameters (pH, eH, and temperature) were measured on site during sample collection using a CTD probe. Water samples were filtered with a 0.22 µm pore size filter (Millipore, Merck KGaA, Darmstadt, Germany) and stored in sterile metal-free plastic tubes in the dark at 4°C until further analysis. Major anions and cations in the water were measured on a Dionex ICS-3000 (Thermo Scientific, Waltham, MA, USA) ion chromatograph at the University of Geneva.

Further elemental analysis was conducted in the Biogeochemistry Laboratory at the Rosenstiel School of Marine, Atmospheric, and Earth Science. All sample and standard preparations were conducted in Class 100 trace metal workstation in a metal-free ISO Level 7 Clean Room using distilled nitric acid (Savillex Acid Purification System, DST-1000) and 18MΩ MilliQ water. The concentration of As in the water sample was determined using a standard addition method following the procedure recommended by Yang et al. ([2018](#)). In brief, a 50 µg.L^{-1} As spike solution was created by diluting NIST-traceable SPEX CertiPrep Solution 2A with 0.16 M ultratrace HNO$_3$. A seawater certified reference material (CASS-6, NRC Canada) was diluted gravimetrically by a factor of 10× with 0.16M ultratrace HNO$_3$, resulting in a diluted seawater solution with 0.1 µg.L^{-1} As. Next, the spike solution was added in variable proportions to six aliquots of this seawater to create a range from 0.1 to 1.8 µg.L^{-1} As. Analysis of this suite of spiked CRM solutions was performed using a triple quadrupole inductively coupled

plasma mass spectrometry (Agilent 8900 ICP-QQQ) using a UHMI setting of 25. The instrument setup included an integrated autosampler (SPS-4) with HEPA filtration and covertkit, Ni skimmer and sampler cones, and a standard electron multiplier detector. During the analysis, the instrument was operated using Mass Hunter 4.5 Workstation Software (C.01.05). Each measurement was performed in triplicate, with 100 sweeps each, and all reported values had less than 5% Relative Standard Deviation (RSD). Prior to each analysis, instrument tuning was conducted using a tuning solution containing 1 μg.g^{-1} Li, Y, and Tl from Agilent Technologies Tuning solution to optimize the signal sensitivity and peak resolution at low, mid, and high m/z ranges. To monitor interference, plasma-derived oxides and doubly charged ions were checked before each analytical batch and maintained below 2% and 3%, respectively. Scandium was introduced using Agilent's in-line internal standard kit as an internal standard to monitor instrument drift throughout the analysis. The measurement of As was performed using the mass shifted O_2 gas mode ($^{75}As \rightarrow ^{91}As$). Sample counts were corrected for contributions from the blank solution by analyzing an acid blank prepared from the same 0.16M HNO_3 used to prepare the CASS-6 seawater dilutions. Counts measured for each of the seven CASS-6 solutions were then regressed against the expected concentrations in the spike of each standard solution. The resulting curve was characterized by a linear relationship ($R^2 = 0.9968$), and the intersection of this curve with the x-axis provided the concentration of As in the unspiked standard reference material (CASS-6) with 96% recovery. Using this CASS-6 verified external 7-point calibration curve, we calculated the concentration of As in the Dead Sea water sample based on measured counts. The detection limit, calculated by the Mass Hunter Software for this analysis was 0.06 μg.L^{-1}.

To analyze the bulk microbial mat composition, approximately 100 mg of freeze-dried and powdered samples were weighed into pre-cleaned 30 mL perfluoroalkoxy alkane (PFA) digestion vessels (Savillex, USA). As previously described, a two-step sequential digestion protocol was conducted using ultra-trace grade 30% H_2O_2 and 16M distilled HNO_3 as described previously (Abdool-Ghany et al., 2023). First, approximately 3 mL of ultratrace H_2O_2 was added to the PFA vessel, the lid was tightly capped, and put on a hot plate set to 115°C for 24 hr. After cooling, the PFA vessels were weighed again to assess mass loss during digestion, which was less than 1.7% on average. Samples were uncapped and put on a hotplate set to 70°C in a metal-free Class-100 workstation to evaporate H_2O_2. Next, 3 mL of 16M distilled HNO_3 was added to each vessel. After tightly capping, the sample weights were recorded again, and the vessels were placed on a hotplate set to 135°C for 48 hr. After cooling, the sample weights were recorded, and the samples were again placed to evaporate on a hotplate set to 70°C. The residual sample was resuspended in 5 mL of ultra-trace 0.16M HNO_3, and aliquots were diluted volumetrically for analysis of elemental concentrations. Procedural blanks, NIST-Traceable SPEX CertiPrep solutions, and certified reference materials (FEBS-1, NCS-DC-73340, IAEA 413, IAEA 392, DOLT-5) digested in the same manner as the samples were analyzed with every batch of samples to confirm accuracy. Average CRM recovery and detection limit for each element are indicated in Table S1 of the Supporting Information S1. Based on replicate analyses of certified reference materials, measurement accuracy was within ±4.5% of certified reference values on average. Analyses were conducted on a triple quadrupole inductively coupled mass spectrometer (Agilent 8900 ICP-QQQ, Agilent, Santa Clara, CA, USA) using a UHMI setting of 8 in He-gas mode on mass for ^{24}Mg and ^{55}Mn, H_2 gas mode for ^{40}Ca, and in O_2 mass shift mode for ^{32}S, ^{75}As, and ^{56}Fe. Scandium was introduced as an on-line internal standard via the Agilent ISTD kit, and plasma-derived oxides and doubly charged ions were maintained below 2% and 3%, respectively, as described above.

2.5. Particle-Induced X-Ray Emission (PIXE) Imaging

Experiments were performed on the resin-embedded sample at the AIFIRA Facility (LP2i-Bordeaux, France) with a 3 MeV proton microbeam (Beam diameter = 1 μm, Beam current ∼ 100 pA). The fast raster of the beam allowed elemental mapping of few mm square areas. μPIXE were done with Si(Li) detectors (Raypsec Ltd, High Wycombe, UK) equipped with a Carbon Funny Filter (thickness 500 μm, hole size 2 mm), which detects X-rays emitted from the interaction of protons with the samples. The beam current was set to keep deadtime below 10% on the PIXE detector. μRBS (Rutherford Backscattering spectroscopy) was performed with a Silicon PIPS detector (Mirion Technologies, Inc., Atlanta, GA, USA), which detects backscattered protons and is used for quantification. Data treatment and quantification were done with SIMNRA 7.02 (www.simnra.com) and GUPIXWIN 2.2.1 (http://pixe.physics.uoguelph.ca/gupix/main; Campbell et al., 2010). Maps and image analyses were obtained using combined imageJ and R protocols. The relative gray scale intensity was transformed into a matrix of values for each pixel using the "image to result" command in ImageJ (V. 1.53e), and then processed as surface plots. Pixel matrices were processed and analyzed for each element with R using the raster and rasterVis packages.

2.6. Synchrotron-Based X-Ray Fluorescence and XANES Spectra Analyses

The resin embedded sample was brought to the Swiss Light Source at the Paul Scherrer Institute, Villingen, Switzerland. Synchrotron-based scanning XRF and absorption contrast were performed at the microXAS beamline using an X-ray energy of 12 keV focused to 1×1 µm^2 using a Kirkpatrick–Baez mirror system. The scans were recorded in the fly scan mode, recording the full XRF spectra every 100 ms with variable step size. The XRF spectra were recorded with single-element silicon drift detectors (Ketek GmbH, Germany) coupled to FalconX pulse processors (XIA LLC, USA). XRF data were fitted using PyMCA (Solé et al., 2007). X-ray absorption near edge structure (XANES) were collected around the following As K-edge regions and step sizes: 11.839–11.86 keV at 0.001 keV steps, 11.86–11.88 at 0.0004 keV steps, 11.88–11.90 at 0.001 keV steps, 11.9–11.95 at 0.002 keV steps and 11.95–12.1 at 0.003 keV steps. Data processing was done with the software Athena (Ravel & Newville, 2005), using the corresponding normalization and background removal parameters: $E0 = 11{,}867.5$ eV, 3rd normalization order, pre-edge range -28.522 to -17.110, flatten normalized data and normalization range between 58.490 and 229.190, with 464,237.57 edge steps. Rbkg was at 1.0 and K-weight at 2. Spline ranges were set between 0 and 7.767 in k, and s0 to 230.01978 in E. XANES measurements were performed five times each point, which induced modifications of the spectrum over time by the beam. For this reason, all spectra presented here are from the first acquisition at each location. An example of the beam-induced transformation is shown in Figure S1 of the Supporting Information S1.

Redox maps were constructed after obtaining XRF maps for arsenic at the following energies: 11,850, 11,868, 11,873, 11,880, and 11,890 eV. Noise on these images was removed on imageJ using the "despeckle" prompt and then divided by the "image calculator" prompt.

The relative gray scale intensity of the XRF map images was transformed into a matrix of values for each pixel using the "image to result" command in ImageJ (V. 1.53e). Pixel matrices were then processed and analyzed for each element with R using the raster and rasterVis packages.

Arsenopyrite (solid mineral), As_2S_2 powder (Arsenic(II) sulfide, Sigma-Aldrich, Merck KGaA, Darmstadt, Germany), As_2O_3 powder (As(III) oxide, Thermo Scientific Chemicals, Waltham, MA, USA), As_2O_5 powder (As (V) oxide, metal base, Thermo Scientific Chemicals, Waltham, MA, USA), and triphenylarsine powder (As(III) $(C_6H_5)_3$) (Thermo Scientific Chemicals, Waltham, MA, USA) were used to obtain reference XANES spectra. Powders were mixed with boron nitride and mounted in nearly 2 mm-thick plexiglass frames.

2.7. Hyperspectral Imaging of Bacterial Pigments

The resin-embedded samples were scanned by a hyperspectral Specim PFD-CL-65-V10E linescan camera (Specim, Oulu, Finland) following the method of Butz et al. (2015). The scanning resolution that is, the pixel size was 60 µm. We examined the sample and the resin for their spectral absorption to identify pigments. The Relative Absorption Band Depth (RABD) in certain wavelength ranges was calculated from the spectra to quantify relative changes in pigments throughout the sample. RABD620 represents phycocyanin, a pigment produced by cyanobacteria (Sorrel et al., 2021). RABD660-670 is interpreted as total chloropigments-a, which represents total algal abundance (Butz et al., 2017; Rein & Sirocko, 2002; Zander et al., 2022). The spectral absorption of the surrounding resin was determined and used as background in the calculation to remove any potential matrix effect of the resin on the sample spectra.

2.8. 16S rRNA Gene and Metagenomic Analysis of Arsenic-Related Genes

Several samples from the Dead Sea pool system were extracted using the DNeasy PowerBiofilm® Kit (Qiagen, Germantown, MD, USA) following the instructions provided by the company. Each sample corresponded to one single mat found in this sinkhole system. Genomic results presented below are from only one mat (i.e., one sample), as described in Section 2.1. The rest of the data set will be published elsewhere. The extracts were quantified using an Invitrogen Qubit ds DNA HS assay kit (Life Technologies, #Q32851, Grand Island, NY, USA), and sent for the amplification of the 16S rRNA gene to Fasteris (Genesupport SA, Geneva, Switzerland) using the primers 515F (5'-GTGYCAGCMGCCGCGGTA-3') and 909R (5'-CCCCGYCAATTCMTTTRAGT-3') (Wang & Qian, 2009). Samples were then purified, quantified, pooled for library preparation (no PCR cycle to finish the library) and sequenced by Illumina Miseq (1 paired-reads run 2×300 bp; Illumina Inc San Diego, CA, USA). Yield and quality controls were within specifications. Samples were then filtered and trimmed using

cutadapt (Martin, 2011), assembled and checked for chimeras using dada2 (Callahan et al., 2016) and further analyzed using phyloseq (McMurdie & Holmes, 2013) and vegan (Oksanen et al., 2007) packages with R (R Core Team, 2013), as described in the Open Research Statement below.

Metagenomes were obtained from the same extracts using Illumina NovaSeq S4 (2 × 150; Illumina Inc San Diego, CA, USA) after shotgun Library Prep at the Rush University Genomics and Microbiome Core Facility. Genomic DNA samples were prepared for sequencing by an initial quantification using a Qubit 4 Fluorometer (Life Technologies, #Q32851, Grand Island, NY, USA). Library preparation was performed using the Illumina DNA Prep Workflow with UDI indexing (#20018705, 20027213 Illumina Inc San Diego, CA, USA) according to the manufacturer's instructions with 50 ng template input and 5 cycles of PCR. An equal-volume pool of all libraries was then created. The pool was quantified using a Qubit DNA High Sensitivity kit (Life Technologies, #Q32851, Grand Island, NY, USA), and the size distribution was assessed using an Agilent 4200 TapeStation System (Agilent Technologies, G2991AA, Santa Clara, CA, USA) using TapeStation D5000 ScreenTape, ladder and assay (Agilent Technologies, #5067–5588, 5067–5590 and 5067–5589, Santa Clara, CA, USA). The pooled libraries were run on an Illumina MiniSeq instrument using a MiniSeq Reagent MO Kit (300 cycles) (Illumina Inc San Diego, CA, USA) run for quality control and library balancing purposes. A new pool was made based on the MiniSeq run results, quantified same as described above, and sequenced on an Illumina NovaSeq 6000 instrument (300 cycles) (Illumina Inc San Diego, CA, USA), with a 1% phiX spike-in. Raw sequence reads were quality trimmed and filtered using Trimmomatic (v0.39) (Bolger et al., 2014) and assembled de novo using SPAdes (v 3.13) (Bankevich et al., 2012) using the –meta option for metagenomic assembly. Reads from each sample were mapped to the assembled contigs of each file using BBmap (sourceforge.net/projects/bbmap/) and converted to sorted BAM files using SAMTools (Danecek et al., 2021). The depth profiles for each assembly were generated using the jgi_summarize_bam_contig_depths tool provided with Metabat2 (Kang et al., 2015). Binning was done using Metabat2 (v 2.15) (Kang et al., 2015) using the default setting. Completeness and contamination of genomes was estimated with CheckM tool (v2) (Parks et al., 2015). Taxonomic classification of metagenomic bins was performed using GTDB-Tk (v 2.1.1) (Chaumeil et al., 2020). Annotation of bins was done with Prokka V (Seemann, 2014), BlastKoala (Kanehisa et al., 2016) and EggNOG-mapper v (Cantalapiedra et al., 2021). To obtain the annotation of proteins found in unbinned contigs, open reading frames were called using Glimmer (Delcher et al., 2007) from the assembly result and subsequently annotated using GhostKoala (Kanehisa et al., 2016) and EggNOG-mapper (Cantalapiedra et al., 2021).

3. Results

3.1. Microbial Mat Composition

The microbial mat consisted mostly of organic matter (Figure 1e), which is loosely grouped under the term EPS, as described by Flemming et al. (2016), and encompassing a wide variety of organic molecules secreted by microbial cells and structuring a community in a biofilm. It included pigment-rich EPS, with occasional localized mineral clusters (upper right corner, Figures 2a and 2b), and more isolated detrital minerals and concretions (Figure 2c). The sample was partially mineralized on its surface, as could be seen by the orange to brownish pustular structures in the hand samples (Figure 1e). These minerals had a blue autofluorescence when viewed using a DAPI filter (excitation 350–400 nm; emission 420–480 nm), which is typical of calcium carbonates (Figures 2a and 2b) further identified as aragonite by Raman Spectroscopy (not presented here). These mineralized areas occurred in the upper right corner of the sample section (Figure 2a) in rather heterogeneous lithofacies composed of aragonite needles partially to completely agglomerated as concretions reaching ~100 μm in length (Figure 2b, Figure S2 in Supporting Information S1). In this mineralized region of the sample (Figure 2b), organic matter is more dispersed as supported by low yellow to red autofluorescence (filters for Rhodamine and APC) compared to the rest of the investigated sample, that is largely structured by microbially secreted EPS.

High-resolution epifluorescence imaging (Figure S2 in Supporting Information S1) revealed a common occurrence of dinoflagellates and diatom shells in the top 5 mm of the sample. The sample also presented cavities and voids (dark blue to black in Figure 2), observed particularly in the middle of the sample, possibly triggered by the resin hybridization protocol. Filaments of various lengths and diameters were present all along the sample, displaying red and yellow autofluorescence (using APC and Rhodamine filters). These filaments were either structureless, organized around voids, or observed in well-ordered parallel laminae. The resulting filamentous network formed well-identifiable wavy textures (see Figure 2c, and in the bottom part of the sample, Figures 1e
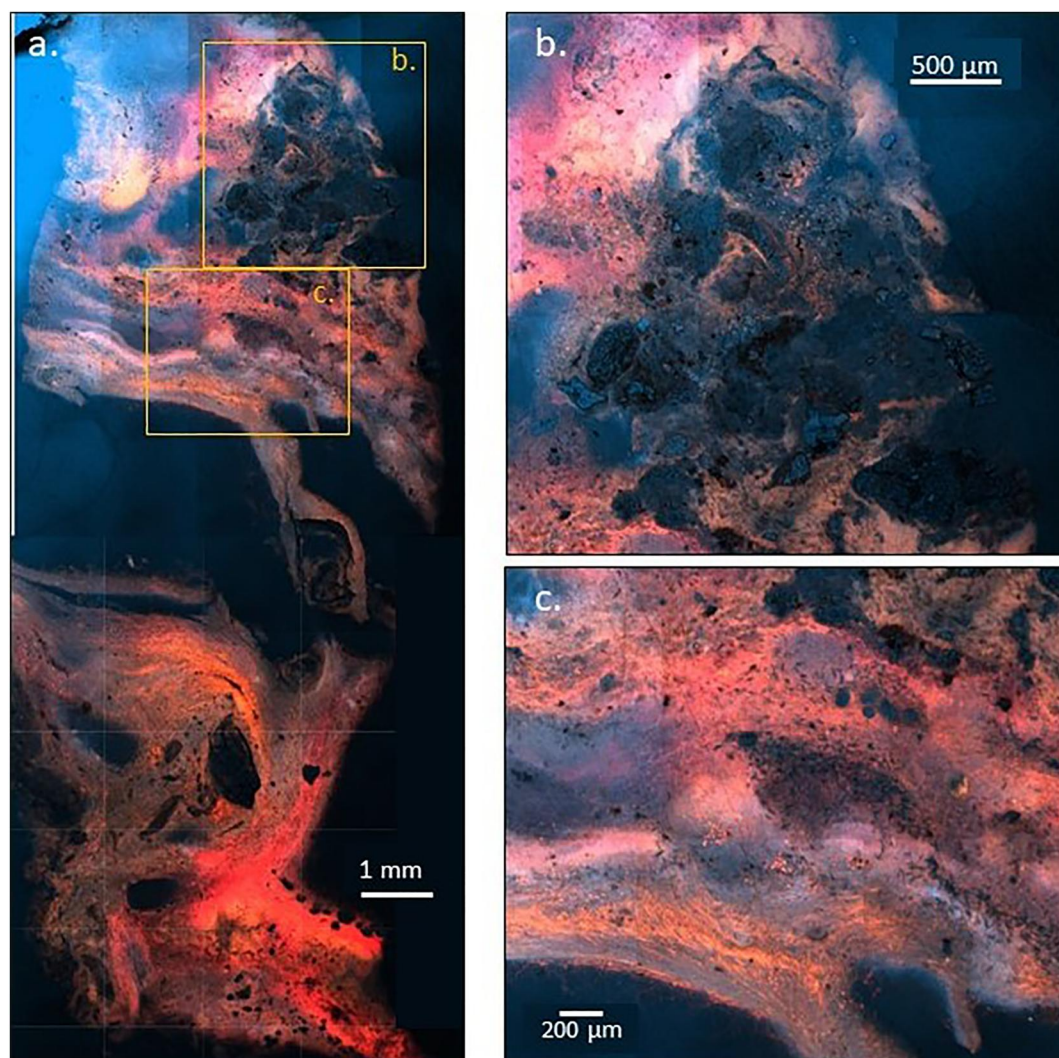
Figure 2. Epifluorescence microscopy images of the microbial mat from the surface of the microbial mat (top of image (a)) to the bottom of the mat (bottom of the section in (a)). The unstained mat was imaged using a combination of the following filters (filter for DAPI: blue color showing autofluorescence of calcium carbonate minerals; filter for APC: red color covering autofluorescence of chlorophyll, allophycocyanin and phycocyanin; filter for Rhodamine: yellow color covering autofluorescence of cyanobacterial phycoerythrin and phycoerythrocyanin). The stacked images highlight most photosynthetic pigments in yellow-red, while minerals (mainly aragonite) are colored in blue. (b) Zoom in the frame labeled (b) in photo (a). (c) Zoom in the frame labeled (c) in photo (a).

and 2a). Coccoids, interpreted here as *Cyanobacteria* based on autofluorescence, occasionally formed denser aggregates. Photopigments were identifiable all the way down the core, with higher autofluorescence observed at the bottom. This downward trend of autofluorescence intensity was confirmed by hyperspectral images (Figures S3 and S4 in Supporting Information S1) of chlorophyll *a* and *b*, and phycocyanin. Overall, yellow-red auto-fluorescence visualized the EPS content and the structure of the mat, while blue (Figures 2b and 2c) represented carbonate minerals, as confirmed by Mg and Si mapping that are commonly enriched in EPS of the Dead Sea system (Figure S5 in Supporting Information S1). In the bottom part of the sample, these blue zones were less present and large black patches/islands showed detrital minerals (silicates).

3.2. Elemental Distribution and Local Chemical Enrichment

Synchrotron-based XRF indicates that As is enriched in most of the EPS but to varying degrees across the sample (Figure 3). The As content reaches a maximum of 15,700 ppm in the middle lamina (arrows Figures 3
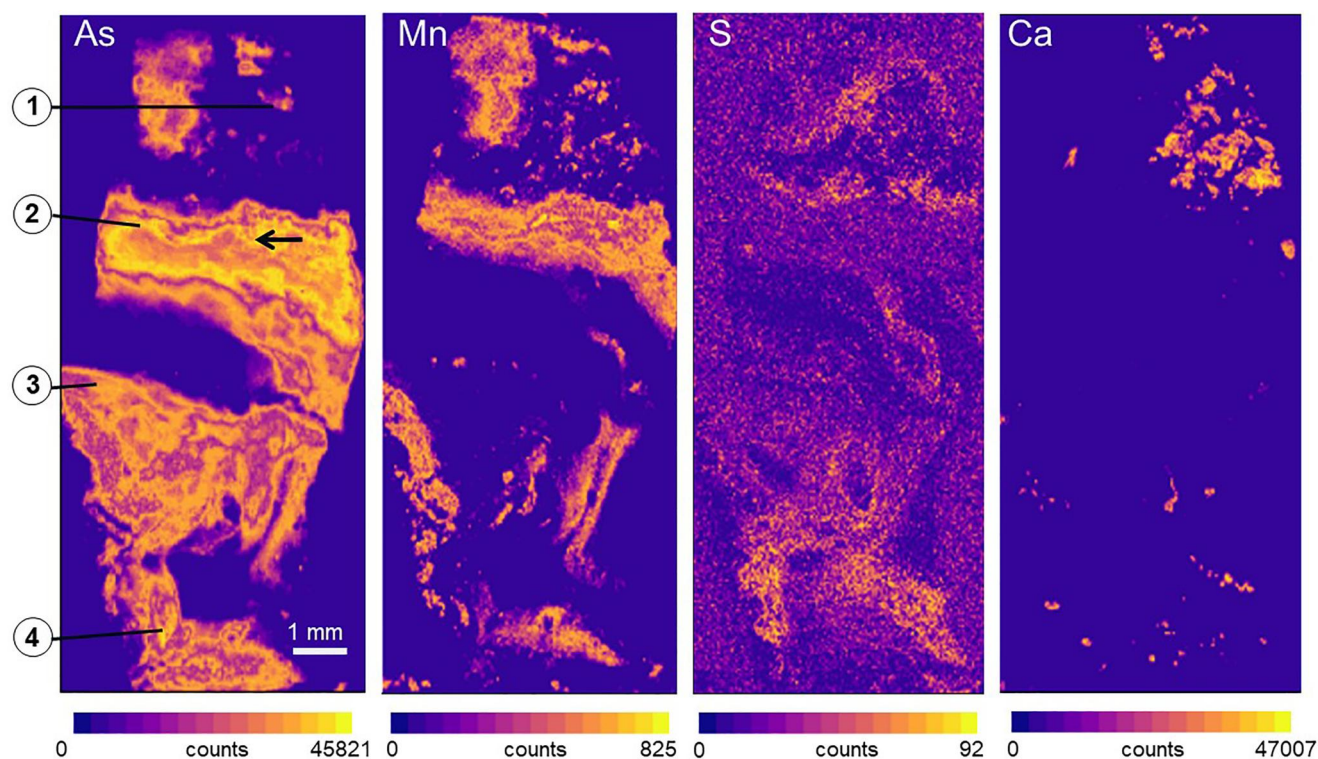
Figure 3. Synchrotron-based XRF maps of the microbial mat showing strong As enrichment associated to a certain extent with Mn concentrations. CaCO minerals are mainly located in the top right corner and associated with Ni and K (not shown). Sulfur increases in the bottom of the mat but has relatively low overall concentrations. The color scale indicates the XRF intensities from the detection limit (purple) to the maximum measured (yellow). The black arrow in the As frame shows the location of the PIXE analyses presented in Figure 4, and numbers correspond to XANES analysis points (Figure 5).

and 4), much higher than other trace elements (e.g., Mn: 2,200 ppm, Fe: 660 ppm; Table 1). The As concentration was more than $390\times$ the bulk concentration measured for the whole sample (40.1 ppm; Table 1), and more than 6.5 million$\times$ the concentration measured in the water from pool 1 at the time of sampling (2.39 $\mu g.L^{-1}$; Table 1). Manganese was often co-enriched with As in many occurrences in the mat, particularly in the max-As layer (Figure 3), where it reached a factor of $5\times$ compared to the bulk sample composition (389.3 ppm Mn). Sulfur enrichment in the As-rich layer was relatively minor ($2.5\times$ compared to the bulk at 7,126.5 ppm S) and reached a maximum in the bottom part of the mat. Calcium was mapped only within mineral phases in Figure 3, but Ca-enrichment was also observed in the EPS (Figure 4), although it did not correlate with the As-Mn-rich phase.

Over 20 XANES spectra were acquired across the sample. They showed similar patterns with a white line peak energy consistently measured at 11,872.4 eV and a single peak shape, as shown for the four points spread from the top to the bottom part of the mat (Figures 3 and 5). The curve shape of all measured points is relatively similar to that obtained for As_2O_5 but with a difference in the As white line peak energy (measured at 11,874.9 eV). The obtained white line peak energies for the standards are 11,871.2 eV for As_2O_3, 11,869.9 eV for AsS_2 and 11,872.4 eV for triphenylarsine. The peak energy of the triphenylarsine is thus identical to the peak energy of the points measured throughout the sample, although the shape of the curve is radically different. These data are presented in Figure 6 and compared to other published white line peak energies for common reference material, including organoarsenic compounds that were not measured during this study but are more commonly found in the environment. Based on these comparisons, the white line measured in this study better matches that of a combination of As(V) organoarsenic species. Values obtained from methylated arsenate (in particular tetramethylarsonium) overlap or are very close to those measured across the mat. Other organoarsenic species, such as arsenobetaine and choline, also show close white line peak energy values but published spectra differ in overall shapes, as discussed in the next sections. Published examples of As(V) organic compounds like methylarsonate, dimethylarsinate and trimethylarsine oxide (MMA(V), DMA(V) and TMAO respectively) show similar shapes,
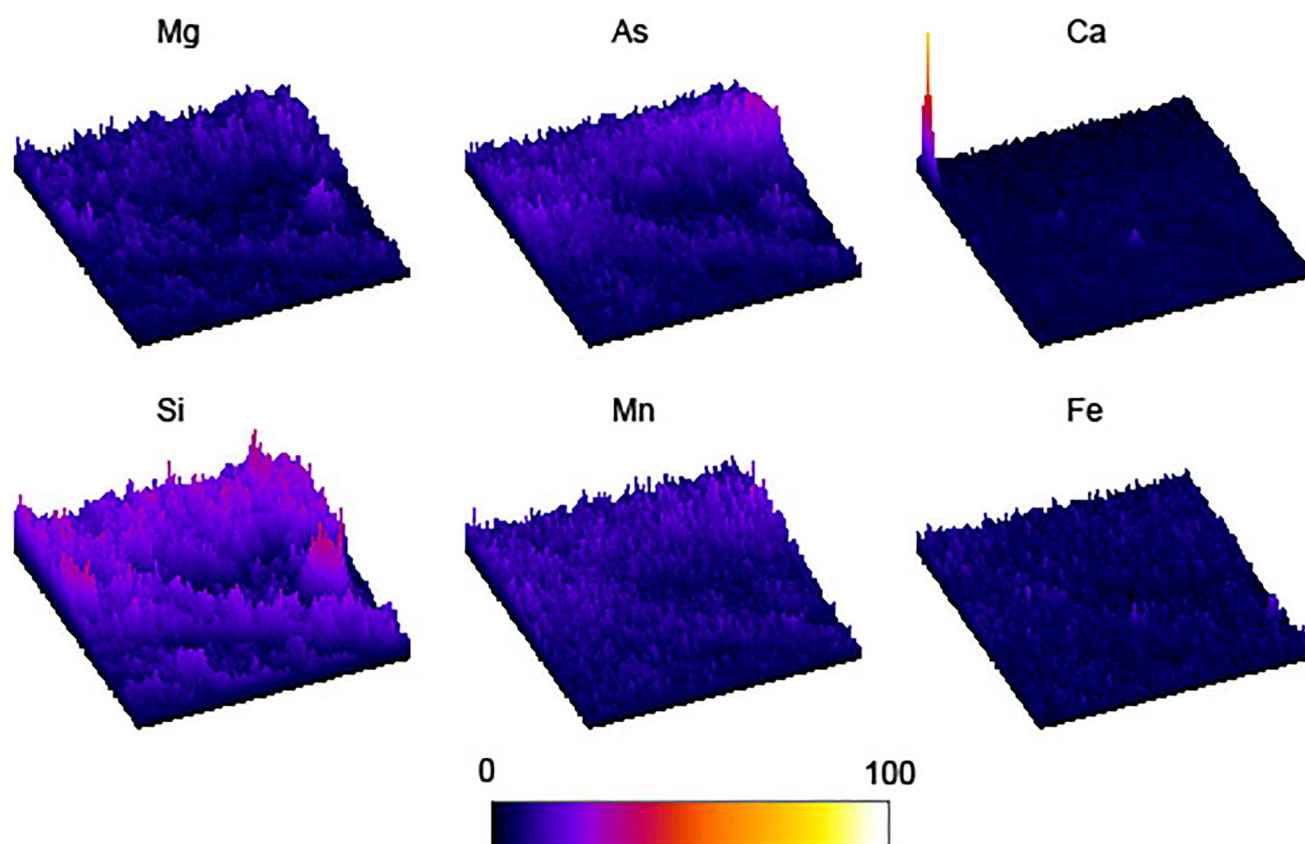
Figure 4. Surface plot of elemental concentrations measured by PIXE mapping in the As-rich zone (arrow in Figure 3). It shows co-enrichment in Si, As, Mn, and Mg. Fe and Ca were also detected. The PIXE spectra also show peaks of, S, Cl, K, Br, Rb, and Sr (see Figure S6 in Supporting Information S1). Images are 250 μm × 250 μm. The color scale shows relative intensity below the detection limit (black) to maximum (white) values.

with a high intensity peak followed by a linear behavior between 11,875 and 11,900 eV, and maximum energy peaks that may contribute together to the observed wide peak measured in the mat (Jahrman et al., 2022; Smith et al., 2005). Arsenic mapping at 11,868 eV (representative of As(III)) and 11,873 eV (representative of As(V)) generally shows similar features dominated by As(V) species (Figure S7 in Supporting Information S1). When compiled in redox maps and count distribution plots, one occurrence in region 2 (As-rich lamina) presents possible co-occurrence of As(III) and As(V) (Figure S7h in Supporting Information S1). Therefore, the contribution of As(III) cannot be ruled out in the XANES spectra of the mat.

Table 1

Chemical Composition of the Mat Water and Bulk Mat (as Measured From Ion Chromatography and QQQ-ICP-MS) and Specific As-Enriched Zone (as Measured by PIXE)

	Water (mg.L^{-1})	Bulk mat ppm (mg.kg^{-1})	As-rich zone (PIXE) ppm (mg.kg^{-1})	EPS to bulk enrichment	EPS to water enrichment
Mg	3.54×10^3	31.8×10^3	152×10^3	4.8	43
Ca	2.20×10^3	166×10^3	25.5×10^3	0.2	12
S	514	7.12×10^3	17.9×10^3	2.5	35
Mn	–	399	2.25×10^3	5.8	–
Fe	–	3.19×10^3	660	0.2	–
As	2.4×10^{-3}	40.1	15.7×10^3	392	6.5×10^6

Note. EPS to bulk enrichment is a ratio between the elements measured in the As-rich zone by PIXE and those measured in the bulk mat. EPS to water enrichment is a ratio between the elements measured in the As-rich zone by PIXE and those measured in the water. Concentrations of sulfur in the bulk mat samples are informational, all other elements were measured using replicate analyses of reference materials (Table S1 in Supporting Information S1).
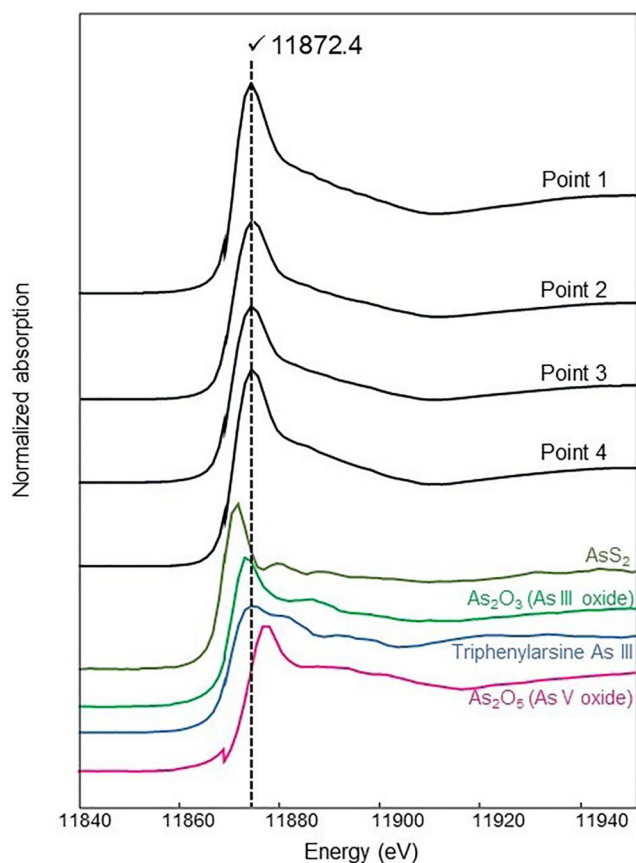
Figure 5. XANES spectra of As across the mat (see Figure 3 for localization), and in reference materials. The broken line refers to the identical white line peak energy (11,872.4 eV) obtained for all points measured throughout the sample.

3.3. Hyperspectral Imaging of Bacterial Pigments

Several spectral absorption troughs in the spectral profiles of the sample as well as of the embedding resins were identified (Figure S3 in Supporting Information S1). The fact that the resin itself has a specific spectral profile means that the resin is absorbing light at certain wavelengths, more specifically at 560–570, 630, 710, 820, 870, and 915 nm. The sample absorbs light at wavelengths of 550, 620, 660, and 915 nm. From these data, the presence of phycocyanin, a pigment produced by cyanobacteria, is observed in the lower part of the sample (Figure S4 in Supporting Information S1, RABD620 in blue). Chlorophyll-*a* and its derivatives represent photosynthetic primary productivity (Figure S4 in Supporting Information S1, RABD660 in dark green). We can state with high confidence that these two pigments are present in the sample as the spectral profile of the resin showed no absorbance at these wavelengths (Figure S3 in Supporting Information S1, panel C) thus causing no interference. The bacteriochlorophyll-c, d, and e (RABD$_{715}$) produced by green sulfur bacteria cannot be assessed as we observe interference with the resin absorption in the same wavelength (Figures S3 and S4 in Supporting Information S1, RABD$_{715}$ and RABD$_{820}$). The resin signal is here represented by one of its several absorption troughs —RABD820 (Figure S4 in Supporting Information S1, RABD$_{820}$). No absorption was observed at the wavelengths specific for the bacteriopheophytin-a, which would show the presence of purple sulfur bacteria. Thus, no anoxic primary producers were found in the sample, only cyanobacterial and photosynthetic primary production.

3.4. Genetic Composition of the Mat

The 16S rRNA gene sequences obtained from this mat show a composition of *Cyanobacteria* predominantly (57%), *Alphaproteobacteria* (17%), *Bacteroidota* (15%), *Chloroflexi* (10%) *Spirochaeta* (4%), and *Gammaproteobacteria* (0.8%). The overall abundance of *Cyanobacteria* matches the observations from the field, smear slides and fluorescence microscopy (Figures 1e and 2). A few phototrophic organisms other than *Cyanobacteria* have potentially been identified within the *Alphaproteobacteria* class as *Rhodobacterales* (0.7%) and *Chloroflexales* (0.7%). Additionally, a few halophilic purple sulfur bacteria affiliated with *Halochromatium* were identified (0.1%). No clade or taxa known to cycle As in a dissimilatory way was identified.
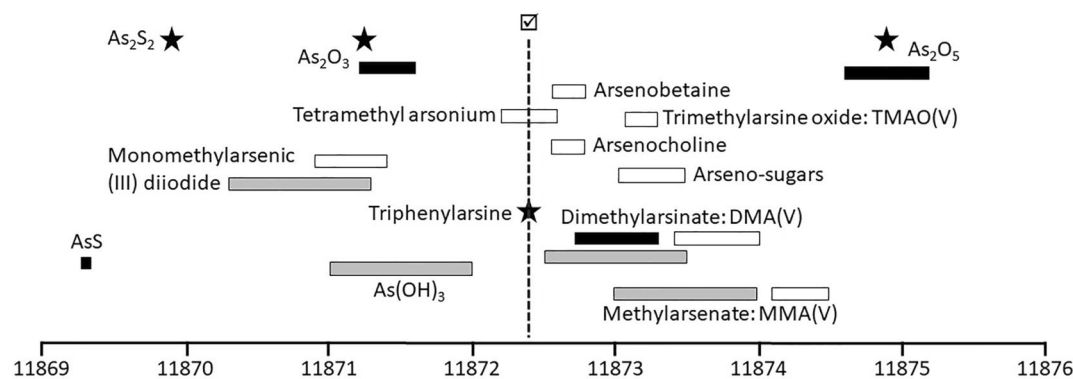
Figure 6. White line energies (in eV) of reference As material including material measured in this study (stars) from Smith et al. (2005; white bars), Bacquart et al. (2007; black bars) and Bacquart et al. (2010; gray bars). The measured whiteline across the mat (see Figure 5) is represented by the broken line and ticked box.

A total of 2,190 metagenomic bins were obtained from the 12 mat samples. The metabolic potential of these organisms will be discussed in a separate study. Genes related to As processing were identified in 94 bins in our microbial mat (pool 1). Of these, 70 were affiliated to the arsenical resistance operon repressor and 20 could be linked to *arsB* arsenite efflux system (including arsenite efflux pump, arsenite-antimonite *arsAB* efflux family transporter, arsenite transmembrane transporter activity, arsenite-activated ATPase *arsA* and arsenical-resistance protein). Additionally, 11 bins contained an arsenate reductase gene, 3 bins associated with the arsenical resistance protein *arsH* encoding for methylarsenite oxidase, and 1 bin associated with As methylase *arsM*. No bin affiliated with any energy-gaining system from As cycling could be found. *Alphaproteobacteria* and *Chloroflexia* had a large number of hits for arsenite efflux systems, but all taxa that could be linked to an As cycle-related bin unsurprisingly had some bins associated with an arsenite efflux system. Finally, arsenate reductase was found for *Alphaproteobacteria*, *Gammaproteobacteria*, *Bacteroidia*, and *Spirochaeta*. *ArsH* was only tied to *Gammaproteobacteria Halothiobacillales* and *Cyanobacteria* (*Synechococcus*), and the *arsM* hit was connected to *Spirochaeta* (*Alkalispirochaeta* genus).

4. Discussion

4.1. Microbial Mat Structure and Composition

At the time of collection, the mat was located at the margin of an active hot spring (Figure 1c). It was in the uppermost pool (pool 1; Figure 1c) of a system consisting of a series of seven pools seemingly connected by a small stream flowing into the Dead Sea. However, no connection could be observed between pool 1 and the other pools. Based on temperatures, salinity and pH, we interpret that pool 1 is likely to be disconnected from the underlying system (pool 2 to pool 7). This fate is experienced by many similar sinkholes in the surrounding area (e.g., pool 1b; Figure 1c) and above, given the rapidly declining Dead Sea level (Al-Halbouni et al., 2021; Nof et al., 2019). This stranding status likely influences the ability to form structured and mineralized mats (which are not observed in the pools below pool 1) and the overall chemical, physical, and biological characteristics of the sample.

The mat is not structured in a continuous isopachous lamina, rather it shows patchy structures, except for the marked horizontal As-rich lamina. Overall, it consists of EPS highly enriched in Mg and Si (Figure 4), a feature observed in EPS of the Dead Sea shores (Thomas et al., 2016). Interestingly, Mg-Si enrichment have been commonly described in (mineralizing) microbial mats (e.g., Arp et al., 2003; Kazmierczak & Kempe, 2003; Kempe et al., 2011) where a transitional Mg-Si phase, often referred to as "amorphous Mg-Si phase", precedes the formation of carbonate minerals (Bontognali et al., 2010; Pace et al., 2018; Zeyen et al., 2015). This enrichment has been interpreted as a transitional phase that enhances biofilm mineralization by $CaCO_3$ precipitation (Pace et al., 2018; Suosaari, Lascu, et al., 2022). In the Dead Sea, heavy Mg enrichment (up to 152,000 ppm) is expected given the extreme concentration of Mg^{2+} in the environment (Ionescu et al., 2012) and in the pond water (Table 1). Silicon concentration is not high in the Dead Sea environment compared to other elements (5.1 mg L^{-1} in average in the water column; Moller et al., 2007), but microbial EPS is commonly enriched in Si, potentially fed by dissolving diatom frustules (present in the mat, Figure S2 in Supporting Information S1). This could explain the high [Si] measured in specific laminae within the mat by PIXE (up to 409,000 ppm, Table 1, Figure 4). Several carbonate precipitates are found in the mat and in this context may result from localized rise of alkalinity that may well be triggered by abiotic processes (Belmaker et al., 2019) or microbial activity (e.g., Glunk et al., 2011).

Redox-sensitive elements (e.g., Mn, Fe, As) are not clearly structured across a depth-gradient along the mat, but rather co-exist at similar levels, pointing to dynamic electron cycling at the mat scale and probably to passive metal binding by EPS, as described by Sforna et al. (2016). Photosynthetic pigments are distributed throughout the sample. It remains to be resolved whether the presence of photosynthetic pigments in the deepest part of the mat is associated with ongoing oxygen production or is a relic of past activity. Interestingly, the maximum presence of phycocyanin and chlorophyll was measured using hyperspectral imaging in a layer lying below 8 mm (Figure S3 in Supporting Information S1). In addition, 16S rRNA gene sequence data show an abundance of anaerobic communities, supporting a complex system structured in dynamic microniches that likely depend on diel cycles and/or alternate spectral niches (e.g., Wong et al., 2015). Organisms involved in oxygenic photosynthesis include phycocyanin and chlorophyll-producing *Cyanobacteria* (Figure 7). Other phototrophic organisms have also been detected, such as carotenoid-bearing heterotrophic *Rhodobacterales* likely involved in the reddish lamina of the mat, filamentous anoxygenic phototrophic of the order *Chloroflexales* (0.7% in the sample,
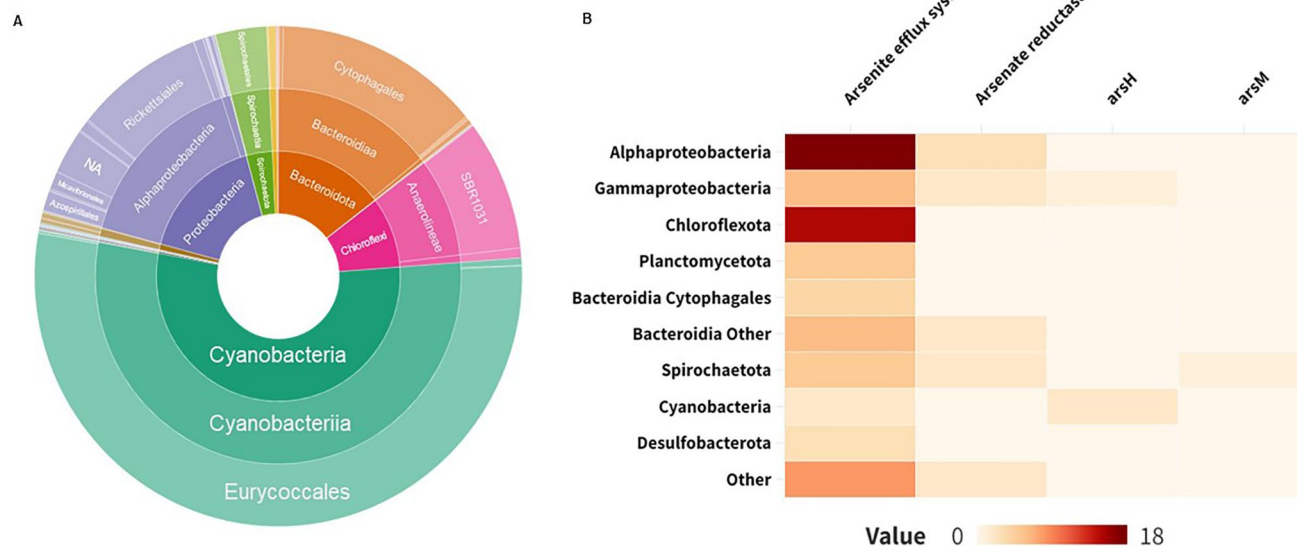
Figure 7. Phylogenetic diversity and As functions of the microbial mat. (a) Genomic affiliation from the microbial mat using 16S rRNA gene sequences and (b) from As-associated genes obtained from metagenomic sequencing, including genes from the arsenite efflux system, arsenate reductase, *arsH* and *arsM*.

Figure 7) and few potentially anoxygenic *Halochromatium* members. Since the genomic data are not depth-resolved, we cannot draw conclusions about the structuring of the microbial mat based on this information. Hyperspectral imaging allows a more detailed localization of specific pigments (chlorophyll vs. phycocyanin, Figure S4 in Supporting Information S1) but does not provide reliable results for bacteriochlorophyll pigments found in anoxygenic phototrophs due to the emission of the acrylic resin employed.

4.2. Arsenic Cycling: No Arsenotrophy but Common Arsenate Detoxification

The absence of arsenotrophic organisms in the 16S rRNA data set does not explain the localization of significant As enrichment, nor does it suggest a link with anoxygenic phototrophic organisms, as observed in the purple mat of Laguna La Brava in the Atacama Desert in Northern Chile (Visscher et al., 2020). Genes that relate to arsenotrophic metabolism (*arr*, *arx*, or *aio*) could not be detected either. Instead, identified As-associated genes point toward common detoxification processes conducted by a variety of organisms. Arsenic resistance in pro-karyotes is generally conferred by an arsenate reductase and the *arsRBC* operon, which provides an overall control for the arsenite efflux system (Andres & Bertin, 2016; Mukhopadhyay et al., 2002). Bins associated with this pathway were widely found in our data set (Figure 7). Our data also show the presence of the less common *arsA*, that makes the efflux more efficient and confers a higher level of As resistance through the *arsRDABC* operon (Bhattacharjee & Rosen, 2007). In the sample, this gene was only found to be associated with *Cyano-bacteria* and one *Euryarchaeota*. Additionally, other *ars* genes linked to organoarsenical detoxification were detected in a limited number of bins and were associated with *arsM* and *arsH*, affiliated with *Spirochaeta* of the *Alkalispirochaeta* genus for *arsM*, *Gammaproteobacteria Halothiobacillales*, and *Cyanobacteria Synechococcus* for *arsH* (Figure 7). The methylation of arsenic is found in all kingdoms, following Challenger's mechanism (Challenger, 1945), which for As involves the reduction of As(V) followed by successive oxidative and reductive methylation steps from As(III), leading to the formation of methylated arsenate and arsenite, and ultimately to its final product DMA(V). Some of these intermediate steps were summarized by Wang et al. (2015) in bacteria, and involve genes like *arsM* and *arsH* (Chen et al., 2015; Qin et al., 2006; Yang & Rosen, 2016). *ArsM* is a microbial arsenite S-adenosylmethionine methyltransferase that catalyzes the formation of methylated compounds from As (III), with volatile trimethylarsine as end product (Qin et al., 2006). In this study, intermediate methylated compounds that have been described corresponded to the low-toxicity TMAO and DMA(V), commonly found as trace As substances in organic tissues (e.g., seafood; Luvonga et al., 2020; Schmidt et al., 2018). The *arsH* gene likely provides resistance to toxic methylated and aromatic As(III) by the oxidation of trivalent organoarsenical compounds derived from herbicides and antimicrobial growth promoters (Chen et al., 2015) into low-toxicity
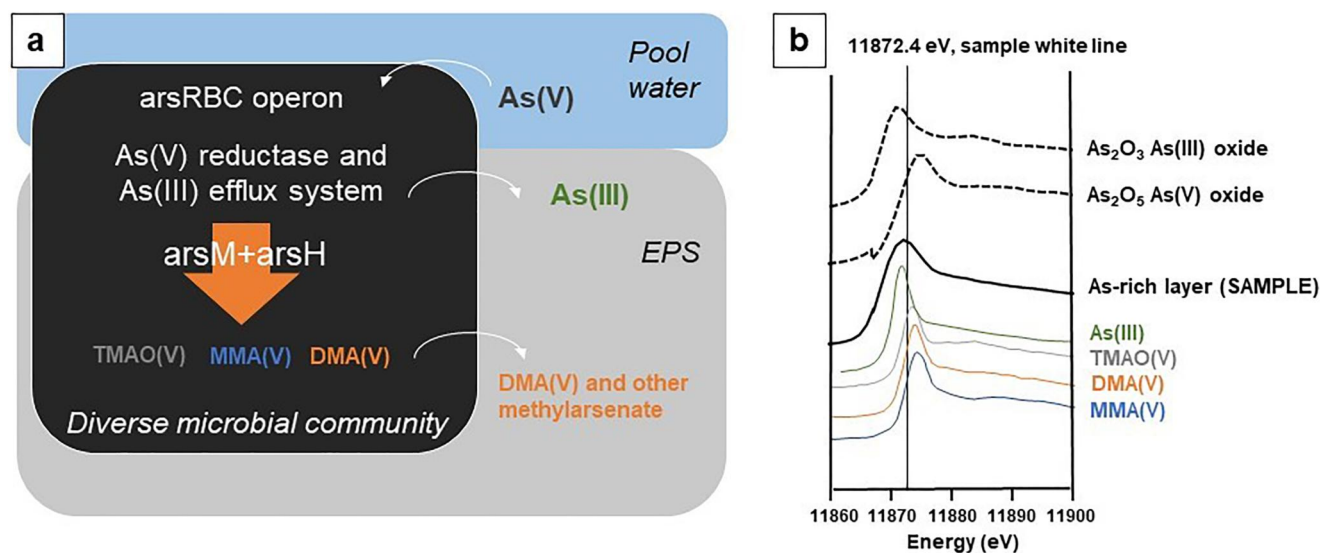
Figure 8. Interpretation of As cycling and species in the Dead Sea mat. (a) Schematic summary of hypothesized As cycling from As(V) rich pool water to immobilization in EPS as organoarsenic. The organoarsenic species DMA(V), TMAO and MMA(V) may be formed through *arsM* and *arsH* genes identified in the metagenomic pool. (b) XANES spectra of putative organoarsenic molecules along with As(III) (all taken from Smith et al. (2005)) with the sample and reference material measured during this study.

pentavalent MMA(V). Therefore, we describe a community potential for As detoxification through arsenate reduction into arsenite and efflux out of the cell, either as arsenite or as As(V) methylated compounds (Figure 8a). In particular, DMA(V) is commonly described as an efflux product for microalgae in aquatic environments (Filella et al., 2023; Wang et al., 2015). The corresponding As molecules that could be expelled based on our data set all have XANES peaks that could contribute together to the signature obtained for the As-rich layer of the pool 1 sample (Figure 8b). Maximum peak energies for the XANES spectra published by Smith et al. (2005) lie between 11,871 eV (for As(III)) and 11,874.5 eV (for MMA(V)), with a one-phased to two-phased post-peak linear descent between 11,875 and 11,900 eV. Comparison of our coupled metagenomic and synchrotron data with published data suggests that such signature could be the result of an efficient detoxification process leading to the efflux and preservation of organoarsenic molecules such as MMA(V), DMA(V), and TMAO, and possibly presence of As(III) in the EPS matrix of the mat (as supported by Figure S7 in Supporting Information S1). The obtained As-rich layer XANES spectrum may well be a combination of the individual XANES spectra of these four species, but no curve fitting could be realized as TMAO(V), DMA(V), and MMA(V) were not used as reference material during our synchrotron experiment.

The As redox state obtained from synchrotron-based redox maps across the mat supports an overall As(V) occurrence throughout the mat (Figure S7 in Supporting Information S1). XANES white lines are in accordance with the presence of As(V) under the form of pentavalent organoarsenics (Figure 6; Bacquart et al., 2007, 2010; Smith et al., 2005). Nevertheless, As(III) cannot be completely ruled out based on XANES signatures, and would be supported by our metagenomic data, which are generally enriched in bins associated with the arsenite efflux system. The stability of this As(III) may however be hindered by the oxic conditions that prevailed in the water of pool 1 at the time of sample collection, and the oxidative effects of putative Mn oxides present in the environment (Ying et al., 2012). Additionally, the overall role of EPS in binding and transforming As is complex. Studies show that EPS production and composition are affected by toxic metalloids such as As (Deepika et al., 2016; Naveed et al., 2020). In particular, Deepika et al. (2016) showed functional and morphological changes for poly-saccharides, proteins and uronic acid of EPS produced by *Rhizobium radiobacter* exposed to As. These compounds all have affinities with, or functional groups able to bind cations (Naveed et al., 2019; Yan et al., 2017). Naveed et al. (2020) reported an increase in EPS production and sorption and transformation of As through binding to specific functional groups for cyanobacteria *Synechocystis*. Some of these transformations involved As(III) oxidation and As(V) reduction in As-spiked solution containing extracted EPS. Such interactions complicate our understanding of As redox cycling and detoxification processes in complex and diverse environments such as our microbial mat.

All data taken together point to a mechanism of As-enrichment in the mat involving the detoxification process through As(V) uptake, reduction to As(III) and methylation in organoarsenic (V) molecules and additional As binding by EPS. The association of manganese with As observed in μPIXE and μXRF remains unexplained. It is likely that environmental Mn oxides influence the oxidation of arsenite released from the cells. Poorly crystalline Mn-oxides were shown to oxidize As(III) at varying levels depending on the Fe(II) content of the medium (Wu et al., 2018). If the waters of pool 1 contain high concentrations of Mn compared to Fe, such chemistry may affect competition between Mn and Fe for As sorption, and favor interaction with Mn. Future analysis of the trace metal composition of water would be useful to elucidate these dynamics.

4.3. Origin and Significance of the Arsenic Signature

The reason for the extreme As enrichment in the mat, together with its spatial restriction to a thin horizontal lamina, remains to be determined. The combined redox (Figure S7 in Supporting Information S1) and metagenomics data (Figure 7b) argue against an arsenotrophic process, which could be fueled by anoxygenic photosynthesis. Arsenotrophy would have produced a different redox state of As associated with specific genes, as observed in environments involving active As-based metabolism (Sancho-Tomás et al., 2018; Visscher et al., 2020). The extreme As concentration measured in the mat of pool 1 is also surprisingly high (15,708 ppm) compared to lower values obtained in the current pool water (0.0024 mg.L^{-1}). Low temperatures compared to neighboring pools support the disconnection of the sampled pool/sinkhole from the hydrological system linking downstream pools. These systems form when circulating groundwater makes its way to the surface through a network of porous environments allowed by the dissolution of the evaporitic substrate. The springs emerge sporadically and may cease fairly quickly or persist for a longer period. The size of the system (ponds and streams) is a function of the intensity of flow, the density of water networks, and the stability of the system (Ionescu et al., 2012; Yechieli et al., 2006). As water flows continuously in a region, it dissolves more minerals and increases the size of ponds and sinkholes. However, many systems can be abandoned due to the rapid dynamics of water circulation powered by seasonal variations in precipitation/evaporation, associated flash floods, and subsurface subsidence that can be generated in the evaporitic and calcareous undergrounds (e.g., Abelson et al., 2017; Al-Halbouni et al., 2021; Yechieli et al., 2006; Zilberman et al., 2017).

Here, we hypothesize that the pond hosting the studied mat has been recently isolated from the local hydrological system, which explains the variation between local As concentrations and the current As concentration in the pond water and the low temperature. Recent stranding could also explain the specific horizontal layering of As enrichment. A potential scenario is that an As-rich water source flowed into this system for a limited time, leading to the production of an As-enriched microbial mat laminae. Regionally, localized and sporadic As enrichment are not uncommon, particularly in fractured bedrock along fault zones (e.g., Sidle et al., 2001), a situation analogous to that of the eastern Dead Sea subsurface. For example, As is found enriched to a similar extent in a dry mat collected a few meters south of pool 1 in a dry sinkhole system (50.19 ppm). One possibility could be that the pulse of arsenic-rich water was accompanied by manganese oxides. In the Dead Sea, Fe is often 10 times more concentrated than Mn in pore water, even in the coastal subsoil (e.g., Nishri, 1984; Nishri & Nissenbaum, 1993). Manganese is believed to originate from the oxidative alteration of Mn-rich carbonates to Mn oxides (Nishri & Nissenbaum, 1993). Mn oxides have been shown to readily oxidize As (III) to As(V) before favoring the sorption of As(V) onto Fe oxides (Ying et al., 2012). Studies of the subsurface behavior of As(V) in relation to sediments also show that dissolved organic matter and Mn oxides compete for As(V) sorption, which can adsorb favorably on organic matter rather than on Mn/Fe oxides (Mohapatra et al., 2006). Finally, the presence of Mg^{2+} or other divalent cations (possibly Ca^{2+}) was shown to favor the adsorption capacity of mineral mixtures of ferruginous and manganous composition (Chakravarty et al., 2002). A combination of these scenarios favored by the response of the microbial community to arsenic may result in combined enrichment of Mn with As (and not other metals, such as Fe, Ni, or Zn) in a specific layer (Figure S8 in Supporting Information S1).

Arsenic enrichment may also be associated with anthropogenic activity in particular from pesticides/herbicides. Keeping in mind that the Dead Sea earned its name on the merit of the scarcity of life forms, pesticides and herbicides are never needed in its vicinity. Anthropogenic sources of arsenic are conceivably carried into the Dead Sea by flashfloods from its relatively large drainage, yet this is not represented in lake brine concentrations. It remains virtually impossible with our current data set to specify the original source of As, be it of organic or inorganic origin. All we can suggest is that a sporadic increase in As concentrations in a spring would have

triggered a protective response to As by microbial mat communities and, therefore, a rapid As-immobilization in the exposed EPS layer. Further mat growth could then carry on. The transient nature of As enrichment in the environment could also be the reason for the lack of evidence of an established arsenotrophic community as observed in stable As-rich environments such the Salar de Atacama, Searles, or Mono lakes (Kulp et al., 2008; Oremland et al., 2017; Visscher et al., 2020).

4.4. Significance for Precambrian Signature

The intensity of As concentrations focused in a millimetric EPS layer of the microbial mat colonizing a Dead Sea pond is remarkable and the development of biotechnological engineering using biofilms for As water decontamination (Ahsan et al., 2012; Singh et al., 2021) presents an interesting area for future research. In some cases, As incorporation may occur through metabolic use, detoxification mechanisms, and arsenotrophy. For instance, in the Salar de Atacama microbialites of Laguna Brava, As (under the form of arsenate and arsenite) was not found to associate with other trace metals, like calcium, silicon, and iron, in organic features, leading the authors to suggest a microbially mediated As cycle, either through detoxification or As-based metabolic pathway (Sancho-Tomás et al., 2018). In the sample from pool 1 in the Dead Sea, synchrotron XRF results showed no co-occurrence of As and other metals except for Mn (Figure 3), which in concert with XANES and metagenomic data suggest a detoxification process rather than As-based metabolic pathways. Thus, we here show that spatially localized As enrichment can occur in mats where no arsenotrophic activity can be detected, implying that other mechanisms beyond arsenotrophy are consistent with intense As enrichment in microbialites. Here, they involve As detoxification by a suite of diverse microorganisms (Figure 7). Such a process could have occurred in Paleoproterozoic settings given the fact that As(III) detoxification processes are considered to have appeared early in the history of life (Chen et al., 2020; Zhu et al., 2014). The case of the 2.7 Ga Tumbiana environment, where independent lines of evidence suggest the presence of oxidative conditions (Eigenbrode & Freeman, 2006; Stüeken et al., 2017; Thomazo et al., 2011), could also be a witness of the first arsenate detoxification processes, since its appearance would have triggered additional stress to the communities (Chen et al., 2017, 2020). The specific dynamics of the Dead Sea provide a setting to observe the formation mechanisms for this kind of biosignature.

Geologically speaking, the potential for such a biosignature to be preserved in the geological archives of the Earth can be complex. Examples from the Tumbiana stromatolites show potential cell remnants and micro-pyrites tightly linked to ancient organic matter laminae bearing specific As enrichment (Marin-Carbonne et al., 2018; Sforna et al., 2014), and well-preserved trace metal-organic associations were indeed found in stromatolites and fossilized biofilms, such as the Dresser Formation stromatolites (Baumgartner et al., 2020). However, this phenomenon of exceptional organic matter preservation appears rare; modern examples of comparable sheet-like microbial mats actively accreting in locations such as Big Pond (Bahamas) or Hamelin Pool (Western Australia) exhibit poor preservation of organic material even at shallow depths (Glunk et al., 2011; Sforna et al., 2016; Suosaari, Lascu, et al., 2022; Suosaari, Reid, et al., 2022). In the microbial mat from the Dead Sea pool presented here, rare $CaCO_3$ concretions found in the As-rich layer of the mat do not contain As (Figure 3). No sulfides are found either in these layers. Organic matter degradation could induce the precipitation of Fe-S minerals given how active the sulfur cycle is in the Dead Sea environment (Häusler, Noriega-Ortega, et al., 2014; Häusler, Weber, et al., 2014; Thomas et al., 2016). Produced sulfide should bind As (Farquhar et al., 2002; Saunders et al., 2018) along with other trace metals such as Cu, Pb, Cd, and Zn, as shown by Moreau et al. (2013). As argued by Reid et al. (2024), the preservation potential of microbial mats is primarily driven by the composition of the initial architecture produced by the mat and the timing of lithification. Organic-rich mats, similar to the one described in this study, contain localized precipitates drowned in organic matter (i.e., Sforna et al., 2016). Taphonomic and/or diagenetic alteration of such organic-rich mats was inferred to result in the formation of packstones or grainstones without obvious microbial contribution to their formation (i.e., laminated fabrics, or preservation of cells; Reid et al., 2024). Consequently, in the case of active microbialites in Big Pond, Bahamas, the preservation of metals (Cu, Zn, Fe, and As) interpreted to be passively sorbed onto EPS (i.e., Sforna et al., 2016) may or may not be preserved in the geological record. Thus, new insights from well-constrained modern microbialite settings regarding the timing and mechanism of elemental enrichment and lithification are crucial for accurate interpretation of the significance of ancient elemental enrichment in microbialites throughout Earth history.

5. Conclusions

The observation of an As-rich microbial mat is the first of its kind in the Dead Sea environment and provides the first evidence of high As concentrations in the vicinity of Dead Sea sinkholes and freshwater springs near the inhabited area of Ein Gedi. Arsenic in the sinkhole and pond water was effectively immobilized in the EPS of the microbial mats. The nature of the As in this EPS has been interpreted as organoarsenic in minimally toxic forms, such as methylated arsenate, but the exact molecules are not fully characterized. Arsenic is not associated with mineral phases, so the fossilization potential of these structures is probably poor, potentially allowing the remobilization of As upon degradation of the mat. We suggest that the As concentration at specific levels in the mat is associated with pulses of As contamination from spring water that have resulted in a detoxification response of the communities present in the mat through efflux and EPS binding. Therefore, this signature is not linked to arsenotrophic processes carried out by microbial communities and is rather of environmental origin, without providing information on energy-gaining metabolism or on the identity of the microbial population. We therefore urge caution in interpreting the As-rich organic matter lamina in modern and ancient stromatolites and fossilized mat structures as irrefutable evidence of arsenotrophy. Here, we showed that As enrichment may not be related to a specific population signature, but rather to the confluence of variable environmental conditions and the dynamic response of a microbial community well-adapted to extreme conditions. Given the important role of the detoxification processes and sorption on EPS, high concentrations of As in microbialites remain a fingerprint of life. However, it is important to recognize that As enrichment in organic matter can inform us about energy-conserving As cycling microbes and can also provide information about chemical gradients or transient enrichment in early life environments. The continued study of well-constrained modern microbialite settings is therefore critical to unraveling the impacts of environmental and microbial influences on the incorporation of chemical biosignatures into microbial deposits that record the evolution of biogeochemical cycles on Earth.

Data Availability Statement

All data and scripts used for this study and necessary for the reproduction of results are available under the Open Science Framework Project available under the identifier https://doi.org/10.17605/OSF.IO/X5F8B (Thomas & Ionescu, 2023). Sequences can be obtained from the NCBI Sequence Read Archive project number PRJNA1078097. A preprint of this study was submitted to EarthArXiv: https://doi.org/10.31223/X5SQ3X.

References

Abdel-Fattah, A., & Pingitore, N. E. (2009). Low levels of toxic elements in Dead Sea black mud and mud-derived cosmetic products. *Environmental Geochemistry and Health*, *31*(4), 487–492. https://doi.org/10.1007/s10653-008-9201-x

Abdool-Ghany, A. A., Pollier, C. G. L., Oehlert, A. M., Swart, P. K., Blare, T., Moore, K., & Solo-Gabriele, H. M. (2023). *Assessing quality and beneficial uses of Sargassum compost*. SSRN.

Abelson, M., Yechieli, Y., Baer, G., Lapid, G., Behar, N., Calvo, R., & Rosensaft, M. (2017). Natural versus human control on subsurface salt dissolution and development of thousands of sinkholes along the Dead Sea coast. *Journal of Geophysical Research: Earth Surface*, *122*(6), 1262–1277. https://doi.org/10.1002/2017JF004219

Abu Ghazleh, S., Hartmann, J., Jansen, N., & Kempe, S. (2009). Water input requirements of the rapidly shrinking Dead Sea. *Naturwissenschaften*, *96*(5), 637–643. https://doi.org/10.1007/s00114-009-0514-0

Adar, O., Groner, E., & Ben Natan, G. (2014). Colonization of a new habitat: The case of the Dead Sea sinkholes-preliminary observations. *Dead Sea and Arava Studies*, *6*(3), 74–89.

Ahsan, N., Faruque, K., Shamma, F., Islam, N., & Akhand, A. A. (2012). Arsenic adsorption by bacterial extracellular polymeric substances. *Bangladesh Journal of Microbiology*, *28*(2), 80–83. https://doi.org/10.3329/bjm.v28i2.11821

Al-Halbouni, D., Watson, R. A., Holohan, E. P., Meyer, R., Polom, U., Dos Santos, F. M., et al. (2021). Dynamics of hydrological and geomorphological processes in evaporite karst at the eastern Dead Sea—A multidisciplinary study. *Hydrology and Earth System Sciences*, *25*(6), 3351–3395. https://doi.org/10.5194/hess-25-3351-2021

Anderson, G. L., Williams, J., & Hille, R. (1992). The purification and characterization of arsenite oxidase from Alcaligenes faecalis, a molybdenum-containing hydroxylase. *Journal of Biological Chemistry*, *267*(33), 23674–23682. https://doi.org/10.1016/s0021-9258(18)35891-5

Andres, J., & Bertin, P. N. (2016). The microbial genomics of arsenic. *FEMS Microbiology Reviews*, *40*(2), 299–322. https://doi.org/10.1093/femsre/fuv050

Arp, G., Reimer, A., & Reitner, J. (2003). Microbialite formation in seawater of increased alkalinity, Satonda Crater Lake, Indonesia. *Journal of Sedimentary Research*, *73*(1), 105–127. https://doi.org/10.1306/071002730105

Bacquart, T., Devès, G., Carmona, A., Tucoulou, R., Bohic, S., & Ortega, R. (2007). Subcellular speciation analysis of trace element oxidation states using synchrotron radiation micro-X-ray absorption near-edge structure. *Analytical Chemistry*, *79*(19), 7353–7359. https://doi.org/10.1021/ac0711135

Bacquart, T., Devès, G., & Ortega, R. (2010). Direct speciation analysis of arsenic in sub-cellular compartments using micro-X-ray absorption spectroscopy. *Environmental Research*, *110*(5), 413–416. https://doi.org/10.1016/j.envres.2009.09.006

Bankevich, A., Nurk, S., Antipov, D., Gurevich, A. A., Dvorkin, M., Kulikov, A. S., et al. (2012). SPAdes: A new genome assembly algorithm and its applications to single-cell sequencing. *Journal of Computational Biology*, *19*(5), 455–477. https://doi.org/10.1089/cmb.2012.0021

Baumgartner, R. J., Van Kranendonk, M. J., Pagès, A., Fiorentini, M. L., Wacey, D., & Ryan, C. (2020). Accumulation of transition metals and metalloids in sulfidized stromatolites of the 3.48 billion–year–old Dresser Formation, Pilbara Craton. *Precambrian Research*, *337*, 105534. https://doi.org/10.1016/j.precamres.2019.105534

Belmaker, R., Lazar, B., Stein, M., Taha, N., & Bookman, R. (2019). Constraints on aragonite precipitation in the Dead Sea from geochemical measurements of flood plumes. *Quaternary Science Reviews*, *221*, 105876. https://doi.org/10.1016/j.quascirev.2019.105876

Bhattacharjee, H., & Rosen, B. P. (2007). Arsenic metabolism in prokaryotic and eukaryotic microbes. In *Molecular microbiology of heavy metals* (pp. 371–406). Springer.

Bolger, A. M., Lohse, M., & Usadel, B. (2014). Trimmomatic: A flexible trimmer for Illumina sequence data. *Bioinformatics*, *30*(15), 2114–2120. https://doi.org/10.1093/bioinformatics/btu170

Bontognali, T. R. R., Vasconcelos, C., Warthmann, R. J., Bernasconi, S. M., Dupraz, C., Strohmenger, C. J., & McKENZIE, J. A. (2010). Dolomite formation within microbial mats in the coastal sabkha of Abu Dhabi (United Arab Emirates). *Sedimentology*, *57*(3), 824–844. https://doi.org/10.1111/j.1365-3091.2009.01121.x

Butz, C., Grosjean, M., Fischer, D., Wunderle, S., Tylmann, W., & Rein, B. (2015). Hyperspectral imaging spectroscopy: A promising method for the biogeochemical analysis of lake sediments. *Journal of Applied Remote Sensing*, *9*(1), 96031. https://doi.org/10.1117/1.JRS.9.096031

Butz, C., Grosjean, M., Goslar, T., & Tylmann, W. (2017). Hyperspectral imaging of sedimentary bacterial pigments: A 1700-year history of meromixis from varved Lake Jaczno, northeast Poland. *Journal of Paleolimnology*, *58*(1), 57–72. https://doi.org/10.1007/s10933-017-9955-1

Callahan, B. J., McMurdie, P. J., Rosen, M. J., Han, A. W., Johnson, A. J. A., & Holmes, S. P. (2016). DADA2: High-resolution sample inference from Illumina amplicon data. *Nature Methods*, *13*(7), 581–583. https://doi.org/10.1038/nmeth.3869

Campbell, J. L., Boyd, N. I., Grassi, N., Bonnick, P., & Maxwell, J. A. (2010). The Guelph PIXE software package IV. *Nuclear Instruments and Methods in Physics Research Section B: Beam Interactions with Materials and Atoms*, *268*(20), 3356–3363. https://doi.org/10.1016/j.nimb.2010.07.012

Cantalapiedra, C. P., Huerta-cepas, J., Hern, A., Letunic, I., & Bork, P. (2021). eggNOG-mapper v2: Functional annotation, orthology assignments, and domain prediction at the metagenomic scale. *Molecular Biology and Evolution*, *38*(12), 5825–5829. https://doi.org/10.1093/molbev/msab293

Caumette, G., Koch, I., & Reimer, K. J. (2012). Arsenobetaine formation in plankton: A review of studies at the base of the aquatic food chain. *Journal of Environmental Monitoring*, *14*(11), 2841–2853. https://doi.org/10.1039/c2em30572k

Chakravarty, S., Dureja, V., Bhattacharyya, G., Maity, S., & Bhattacharjee, S. (2002). Removal of arsenic from groundwater using low cost ferruginous manganese ore. *Water Research*, *36*(3), 625–632. https://doi.org/10.1016/S0043-1354(01)00234-2

Challenger, F. (1945). Biological methylation. *Chemical Reviews*, *36*(3), 315–361. https://doi.org/10.1021/cr60115a003

Chaumeil, P., Mussig, A. J., Parks, D. H., & Hugenholtz, P. (2020). Genome analysis GTDB-Tk: A toolkit to classify genomes with the genome taxonomy database. *Bioinformatics*, *36*(6), 1925–1927. https://doi.org/10.1093/bioinformatics/btz848

Chen, J., Bhattacharjee, H., & Rosen, B. P. (2015). ArsH is an organoarsenical oxidase that confers resistance to trivalent forms of the herbicide monosodium methylarsenate and the poultry growth promoter roxarsone. *Molecular Microbiology*, *96*(5), 1042–1052. https://doi.org/10.1111/mmi.12988

Chen, S. C., Sun, G. X., Rosen, B. P., Zhang, S. Y., Deng, Y., Zhu, B. K., et al. (2017). Recurrent horizontal transfer of arsenite methyltransferase genes facilitated adaptation of life to arsenic. *Scientific Reports*, *7*(1), 1–11. https://doi.org/10.1038/s41598-017-08313-2

Chen, S. C., Sun, G. X., Yan, Y., Konstantinidis, K. T., Zhang, S. Y., Deng, Y., et al. (2020). The Great Oxidation Event expanded the genetic repertoire of arsenic metabolism and cycling. *Proceedings of the National Academy of Sciences of the United States of America*, *117*(19), 10414–10421. https://doi.org/10.1073/pnas.2001063117

Closson, D., & Abou Karaki, N. (2009). Human-induced geological hazards along the Dead Sea coast. *Environmental Geology*, *58*(2), 371–380. https://doi.org/10.1007/s00254-008-1400-3

Danecek, P., Bonfield, J. K., Liddle, J., Marshall, J., Ohan, V., Pollard, M. O., et al. (2021). Twelve years of SAMtools and BCFtools. *GigaScience*, *10*(2), giab008. https://doi.org/10.1093/gigascience/giab008

Deepika, K. V., Raghuram, M., Kariali, E., & Bramhachari, P. V. (2016). Biological responses of symbiotic Rhizobium radiobacter strain VBCK1062 to the arsenic contaminated rhizosphere soils of mung bean. *Ecotoxicology and Environmental Safety*, *134*, 1–10. https://doi.org/10.1016/j.ecoenv.2016.08.008

Delcher, A. L., Bratke, K. A., Powers, E. C., & Salzberg, S. L. (2007). Identifying bacterial genes and endosymbiont DNA with Glimmer. *Bioinformatics*, *23*(6), 673–679. https://doi.org/10.1093/bioinformatics/btm009

Duval, S., Ducluzeau, A. L., Nitschke, W., & Schoepp-Cothenet, B. (2008). Enzyme phylogenies as markers for the oxidation state of the environment: The case of respiratory arsenate reductase and related enzymes. *BMC Evolutionary Biology*, *8*(1), 206. https://doi.org/10.1186/1471-2148-8-206

Edmonds, J. S., Francesconi, K. A., Cannon, J. R., Raston, C. L., Skelton, B. W., & White, A. H. (1977). Isolation, crystal structure and synthesis of arsenobetaine, the arsenical constituent of the western rock lobster Panulirus longipes cygnus George. *Tetrahedron Letters*, *18*(18), 1543–1546. https://doi.org/10.1016/S0040-4039(01)93098-9

Edwardson, C. F., & Hollibaugh, J. T. (2017). Metatranscriptomic analysis of prokaryotic communities active in sulfur and arsenic cycling in Mono Lake, California, USA. *ISME Journal*, *11*(10), 2195–2208. https://doi.org/10.1038/ismej.2017.80

Eigenbrode, J. L., & Freeman, K. H. (2006). Late Archean rise of aerobic microbial ecosystems. *Proceedings of the National Academy of Sciences of the United States of America*, *103*(43), 15759–15764. https://doi.org/10.1073/pnas.0607540103

Farías, M. E., Rascovan, N., Toneatti, D. M., Albarracín, V. H., Flores, M. R., Poiré, D. G., et al. (2013). The discovery of stromatolites developing at 3570 m above sea level in a high-altitude volcanic Lake Socompa, Argentinean Andes. *PLoS One*, *8*(1), e53497. https://doi.org/10.1371/journal.pone.0053497

Farquhar, M. L., Charnock, J. M., Livens, F. R., & Vaughan, D. J. (2002). Mechanisms of arsenic uptake from aqueous solution by interaction with goethite, lepidocrocite, mackinawite, and pyrite: An X-ray absorption spectroscopy study. *Environmental Science and Technology*, *36*(8), 1757–1762. https://doi.org/10.1021/es010216g

Fernandez, A. B., Rasuk, M. C., Visscher, P. T., Contreras, M., Novoa, F., Poire, D. G., et al. (2016). Microbial diversity in sediment ecosystems (evaporites domes, microbial mats, and crusts) of Hypersaline Laguna Tebenquiche, Salar de Atacama, Chile. *Frontiers in Microbiology*, *7*, 1–18. https://doi.org/10.3389/fmicb.2016.01284

Filella, M., Wey, S., Matoušek, T., Coster, M., Rodríguez-Murillo, J. C., & Loizeau, J. L. (2023). Arsenic in Lake Geneva (Switzerland, France): Long term monitoring, and redox and methylation speciation in an As unpolluted, oligo-mesotrophic lake. *Environmental Sciences: Processes & Impacts*, *25*(4), 850–869. https://doi.org/10.1039/d2em00431c

Flemming, H. C., Wingender, J., Szewzyk, U., Steinberg, P., Rice, S. A., & Kjelleberg, S. (2016). Biofilms: An emergent form of bacterial life. *Nature Reviews Microbiology*, *14*(9), 563–575. https://doi.org/10.1038/nrmicro.2016.94

Glunk, C., Dupraz, C., Braissant, O., Gallagher, K. L., Verrecchia, E. P., Visscher, P. T., et al. (2011). Microbially mediated carbonate precipitation in a hypersaline lake, Big Pond (Eleuthera, Bahamas). *Sedimentology*, *58*(3), 720–736. https://doi.org/10.1111/j.1365-3091.2010.01180.x

Häusler, S., Noriega-Ortega, B. E., Polerecky, L., Meyer, V., de Beer, D., & Ionescu, D. (2014). Microenvironments of reduced salinity harbour biofilms in Dead Sea underwater springs. *Environmental Microbiology Reports*, *6*(2), 152–158. https://doi.org/10.1111/1758-2229.12140

Häusler, S., Weber, M., Siebert, C., Holtappels, M., Noriega-Ortega, B. E., De Beer, D., & Ionescu, D. (2014). Sulfate reduction and sulfide oxidation in extremely steep salinity gradients formed by freshwater springs emerging into the Dead Sea. *FEMS Microbiology Ecology*, *90*(3), 956–969. https://doi.org/10.1111/1574-6941.12449

Herbel, M. J., Switzer Blum, J., Hoeft, S. E., Cohen, S. M., Arnold, L. L., Lisak, J., et al. (2002). Dissimilatory arsenate reductase activity and arsenate-respiring bacteria in bovine rumen fluid, hamster feces, and the termite hindgut. *FEMS Microbiology Ecology*, *41*(1), 59–67. https://doi.org/10.1016/S0168-6496(02)00266-0

Hirshberg, O., & Ben-Ami, F. (2019). Sinkholes as a source of life in the Dead Sea region. *Aquatic Sciences*, *0*(0), 0. https://doi.org/10.1007/s00027-018-0611-2

Honschopp, S., Brunken, N., Nehrkorn, A., & Breunig, H. J. (1996). Isolation and characterization of a new arsenic methylating bacterium from soil. *Microbiological Research*, *151*(1), 37–41. https://doi.org/10.1016/S0944-5013(96)80053-X

Ionescu, D., Siebert, C., Polerecky, L., Munwes, Y. Y., Lott, C., Häusler, S., et al. (2012). Microbial and chemical characterization of underwater fresh water springs in the Dead Sea. *PLoS One*, *7*(6), e38319. https://doi.org/10.1371/journal.pone.0038319

Jahrman, E. P., Yu, L. L., Krekelberg, W. P., Sheen, D. A., Allison, T. C., & Molloy, J. L. (2022). Assessing arsenic species in foods using regularized linear regression of the arsenic K-edge X-ray absorption near edge structure. *Journal of Analytical Atomic Spectrometry*, *37*(6), 1247–1258. https://doi.org/10.1039/d1ja00445j

Kanehisa, M., Sato, Y., & Morishima, K. (2016). BlastKOALA and GhostKOALA: KEGG tools for functional characterization of genome and metagenome sequences. *Journal of Molecular Biology*, *428*(4), 726–731. https://doi.org/10.1016/j.jmb.2015.11.006

Kang, D. D., Froula, J., Egan, R., & Wang, Z. (2015). MetaBAT, an efficient tool for accurately reconstructing single genomes from complex microbial communities. *PeerJ*, *3*, 1–15. https://doi.org/10.7717/peerj.1165

Kazmierczak, J., & Kempe, S. (2003). Modern terrestrial analogues for the carbonate globules in Martian meteorite ALH84001. *Naturwissenschaften*, *90*(90), 167–172. https://doi.org/10.1007/s00114-003-0411-x

Kempe, S., Kremer, B., Moreira, D., & Tavera, R. (2011). Hydrochemistry and microbialites of the alkaline crater lake Alchichica, Mexico. *Facies*, *57*(57), 543–570. https://doi.org/10.1007/s10347-010-0255-8

Kotova, I., Kayukova, E., & Kotov, S. (2016). Peloids of Crimean salt lakes and the Dead Sea: Controls on composition and formation. *Environmental Earth Sciences*, *75*(16), 1–14. https://doi.org/10.1007/s12665-016-5999-1

Kulp, T. R., Hoeft, S. E., Asao, M., Madigan, M. T., Hollibaugh, J. T., Fisher, J. C., et al. (2008). Arsenic(III) fuels anoxygenic photosynthesis in hot spring biofilms from Mono Lake, California. *Science*, *321*(5891), 967–970. https://doi.org/10.1126/science.1160799

Lakso, J. U., & Peoples, S. A. (1975). Methylation of inorganic arsenic by mammals. *Journal of Agricultural and Food Chemistry*, *23*(4), 674–676. https://doi.org/10.1021/jf60200a028

Lebrun, E., Brugna, M., Baymann, F., Muller, D., Lièvremont, D., Lett, M. C., & Nitschke, W. (2003). Arsenite oxidase, an ancient bioenergetic enzyme. *Molecular Biology and Evolution*, *20*(5), 686–693. https://doi.org/10.1093/molbev/msg071

Lensky, N. G., Dvorkin, Y., Lyakhovsky, V., Gertman, I., & Gavrieli, I. (2005). Water, salt, and energy balances of the Dead Sea. *Water Resources Research*, *41*(12), 1–13. https://doi.org/10.1029/2005WR004084

Levy, E. J., Thomas, C., Antler, G., Gavrieli, I., Turchyn, A. V., Grossi, V., et al. (2022). Intensified microbial sulfate reduction in the deep Dead Sea during the early Holocene Mediterranean sapropel 1 deposition. *Geobiology*, *20*(4), 1–15. https://doi.org/10.1111/gbi.12493

Luvonga, C., Rimmer, C. A., Yu, L. L., & Lee, S. B. (2020). Organoarsenicals in seafood: Occurrence, dietary exposure, toxicity, and risk assessment considerations—A review. *Journal of Agricultural and Food Chemistry*, *68*(4), 943–960. https://doi.org/10.1021/acs.jafc.9b07532

Marin-Carbonne, J., Remusat, L., Sforna, M. C., Thomazo, C., Cartigny, P., & Philippot, P. (2018). Sulfur isotope's signal of nanopyrites enclosed in 2.7 Ga stromatolitic organic remains reveal microbial sulfate reduction. *Geobiology*, *16*(2), 121–138. https://doi.org/10.1111/gbi.12275

Martin, M. (2011). Cutadapt removes adapter sequences from high-throughput sequencing reads. *EMBnet. Journal*, *17*(1), 10–12. https://doi.org/10.14806/ej.17.1.200

Mcbride, B. C., & Wolfe, R. S. (1971). Biosynthesis of dimethylarsine by methanobacterium. *Biochemistry*, *10*(23), 4312–4317. https://doi.org/10.1021/bi00799a024

McEwan, A. G., Ridge, J. P., McDevitt, C. A., & Hugenholtz, P. (2002). The DMSO reductase family of microbial molybdenum enzymes; molecular properties and role in the dissimilatory reduction of toxic elements. *Geomicrobiology Journal*, *19*(1), 3–21. https://doi.org/10.1080/014904502317246138

McMurdie, P. J., & Holmes, S. (2013). Phyloseq: An R package for reproducible interactive analysis and graphics of microbiome census data. *PLoS One*, *8*(4), e61217. https://doi.org/10.1371/journal.pone.0061217

Mohapatra, D., Mishra, D., Chaudhury, G., & Das, R. (2006). Effect of dissolved organic matter on the adsorption and stability of As(V) on manganese wad. *Separation and Purification Technology*, *49*(3), 223–229. https://doi.org/10.1016/j.seppur.2005.10.003

Moller, P., Rosenthal, E., Geyer, S., Guttman, J., Dulski, P., Rybakov, M., et al. (2007). Hydrochemical processes in the lower Jordan valley and in the Dead Sea area. *Chemical Geology*, *239*(1–2), 27–49. https://doi.org/10.1016/j.chemgeo.2006.12.004

Moreau, J. W., Fournelle, J. H., & Banfield, J. F. (2013). Quantifying heavy metals sequestration by sulfate-reducing bacteria in an acid mine drainage-contaminated natural wetland. *Frontiers in Microbiology*, *4*, 1–10. https://doi.org/10.3389/fmicb.2013.00043

Morita, M., & Shibata, Y. (1990). Chemical form of arsenic in marine macroalgae. *Applied Organometallic Chemistry*, *4*(3), 181–190. https://doi.org/10.1002/aoc.590040303

Mukhopadhyay, R., Rosen, B. P., Phung, L. T., & Silver, S. (2002). Microbial arsenic: From geocycles to genes and enzymes. *FEMS Microbiology Reviews*, *26*(3), 311–325. https://doi.org/10.1016/S0168-6445(02)00112-2

Naveed, S., Li, C., Lu, X., Chen, S., Yin, B., Zhang, C., & Ge, Y. (2019). Microalgal extracellular polymeric substances and their interactions with metal(loid)s: A review. *Critical Reviews in Environmental Science and Technology*, *49*(19), 1769–1802. https://doi.org/10.1080/10643389.2019.1583052

Naveed, S., Li, C., Zhang, J., Zhang, C., & Ge, Y. (2020). Sorption and transformation of arsenic by extracellular polymeric substances extracted from Synechocystis sp. PCC6803. *Ecotoxicology and Environmental Safety*, *206*, 111200. https://doi.org/10.1016/j.ecoenv.2020.111200

Nishri, A. (1984). The geochemistry of manganese in the Dead Sea. *Earth and Planetary Science Letters*, *71*(2), 415–426. https://doi.org/10.1016/0012-821X(84)90107-9

Nishri, A., & Nissenbaum, A. (1993). Formation of manganese oxyhydroxides on the Dead Sea coast by alteration of Mn-enriched carbonates. *Hydrobiologia*, *267*(1–3), 61–73. https://doi.org/10.1007/BF00018791

Nissenbaum, A. (1977). Minor and trace elements in Dead Sea water. *Chemical Geology*, *19*(1–4), 99–111. https://doi.org/10.1016/0009-2541(77)90008-0

Nof, R. N., Abelson, M., Raz, E., Magen, Y., Atzori, S., Salvi, S., & Baer, G. (2019). SAR interferometry for sinkhole early warning and susceptibility assessment along the Dead Sea, Israel. *Remote Sensing*, *11*(1), 5–20. (Figure 1). https://doi.org/10.3390/rs11010089

Oksanen, J., Kindt, R., Legendre, P., O'Hara, B., Stevens, M. H. H., Oksanen, M. J., & Suggests, M. (2007). *The vegan package*. Community Ecology Package, 10.

Oremland, R., & Stolz, J. (2003). The ecology of arsenic. *Science*, *300*(5621), 939–944. https://doi.org/10.1126/science.1081903

Oremland, R. S., Kulp, T. R., Blum, J. S., Hoeft, S. E., Baesman, S., Miller, L. G., & Stolz, J. F. (2005). Microbiology: A microbial arsenic cycle in a salt-saturated, extreme environment. *Science*, *308*(5726), 1305–1308. https://doi.org/10.1126/science.1110832

Oremland, R. S., Saltikov, C. W., Stolz, J. F., & Hollibaugh, J. T. (2017). Autotrophic microbial arsenotrophy in arsenic-rich soda lakes. *FEMS Microbiology Letters*, *364*(15). https://doi.org/10.1093/femsle/fnx146

Oremland, R. S., Saltikov, C. W., Wolfe-Simon, F., & Stolz, J. F. (2009). Arsenic in the evolution of Earth and extraterrestrial ecosystems. *Geomicrobiology Journal*, *26*(7), 522–536. https://doi.org/10.1080/01490450903102525

Oren, A. (1983). Population dynamics of halobacteria in the Dead Sea water column. *Limnology & Oceanography*, *28*(6), 1094–1103. https://doi.org/10.4319/lo.1983.28.6.1094

Oren, A. (1993). The Dead Sea—Alive again. *Cellular and Molecular Life Sciences*, *49*(6), 518–522. https://doi.org/10.1007/bf01955154

Oren, A. (1999). Microbiological studies in the Dead Sea: Future challenges toward the understanding of life at the limit of salt concentrations. *Hydrobiologia*, *405*, 1–9. https://doi.org/10.1023/A:1003879932328

Oren, A. (2010). The dying Dead Sea: The microbiology of an increasingly extreme environment. *Lakes and Reservoirs: Research and Management*, *15*(3), 215–222. https://doi.org/10.1111/j.1440-1770.2010.00435.x

Oren, A., Gurevich, P., Anati, D., Barkan, E., & Luz, B. (1995). A bloom of *Dunaliella parva* in the Dead Sea in 1992: Biological and biogeochemical aspects. *Hydrobiologia*, *297*(297), 173–185. https://doi.org/10.1007/bf00019283

Pace, A., Bourillot, R., Bouton, A., Vennin, E., Braissant, O., Dupraz, C., et al. (2018). Formation of stromatolite lamina at the interface of oxygenic-anoxygenic photosynthesis. *Geobiology*, *16*(4), 378–398. https://doi.org/10.1111/gbi.12281

Parks, D. H., Imelfort, M., Skennerton, C. T., Hugenholtz, P., & Tyson, G. W. (2015). CheckM: Assessing the quality of microbial genomes recovered from isolates, single cells, and metagenomes. *Genome Research*, *25*(7), 1043–1055. https://doi.org/10.1101/gr.186072.114.Freely

Qin, J., Rosen, B. P., Zhang, Y., Wang, G., Franke, S., & Rensing, C. (2006). Arsenic detoxification and evolution of trimethylarsine gas by a microbial arsenite S-adenosylmethionine methyltransferase. *Proceedings of the National Academy of Sciences of the United States of America*, *103*(7), 2075–2080. https://doi.org/10.1073/pnas.0506836103

Ravel, B., & Newville, M. (2005). ATHENA, ARTEMIS, HEPHAESTUS: Data analysis for X-ray absorption spectroscopy using IFEFFIT. *Journal of Synchrotron Radiation*, *12*, 537–541. https://doi.org/10.1107/s0909049505012719

Reid, R. P., Suosaari, E. P., Oehlert, A. M., Pollier, C. G. L., & Dupraz, C. (2024). Microbialite accretion and growth: Lessons from Shark Bay and the Bahamas, *1–25*.

Rein, B., & Sirocko, F. (2002). In-situ reflectance spectroscopy—Analysing techniques for high-resolution pigment logging in sediment cores. *International Journal of Earth Sciences*, *91*(5), 950–954. https://doi.org/10.1007/s00531-002-0264-0

Rosen, B. P. (2002). Biochemistry of arsenic detoxification. *FEBS Letters*, *529*(1), 86–92. https://doi.org/10.1016/s0014-5793(02)03186-1

Saikat, S. Q., Selim, A. M., Kessi, J., Wehrli, E., & Hanselmann, K. W. (2001). Transformation of arsenic compounds by bacteria from groundwater sediments of Bangladesh. Technical report.

Sancho-Tomás, M., Somogyi, A., Medjoubi, K., Bergamaschi, A., Visscher, P. T., Van Driessche, A. E. S., et al. (2018). Distribution, redox state and (bio)geochemical implications of arsenic in present day microbialites of Laguna Brava, Salar de Atacama. *Chemical Geology*, *490*(7), 13–21. https://doi.org/10.1016/j.chemgeo.2018.04.029

Saona, L. A., Soria, M., Durán-Toro, V., Wörmer, L., Milucka, J., Castro-Nallar, E., et al. (2021). Phosphate-arsenic interactions in halophilic microorganisms of the microbial mat from Laguna Tebenquiche: From the microenvironment to the genomes. *Microbial Ecology*, *81*(4), 941–953. https://doi.org/10.1007/s00248-020-01673-9

Saunders, J. A., Lee, M. K., Dhakal, P., Ghandehari, S. S., Wilson, T., Billor, M. Z., & Uddin, A. (2018). Bioremediation of arsenic-contaminated groundwater by sequestration of arsenic in biogenic pyrite. *Applied Geochemistry*, *96*, 233–243. https://doi.org/10.1016/j.apgeochem.2018.07.007

Schmidt, L., Landero, J. A., Novo, D. L. R., Duarte, F. A., Mesko, M. F., Caruso, J. A., & Flores, E. M. M. (2018). A feasible method for As speciation in several types of seafood by LC-ICP-MS/MS. *Food Chemistry*, *255*, 340–347. https://doi.org/10.1016/j.foodchem.2018.02.079

Schoepp-Cothenet, B., Duval, S., Santini, J. M., & Nitschke, W. (2009). Comment on "Arsenic (III) fuels anoxygenic photosynthesis in hot spring biofilms from Mono Lake, California.". *Science*, *323*(5914), 583. https://doi.org/10.1126/science.1164967

Seemann, T. (2014). Prokka: Rapid prokaryotic genome annotation. *Bioinformatics*, *30*(14), 2068–2069. https://doi.org/10.1093/bioinformatics/btu153

Sforna, M. C., Catherine, M., Philippot, P., Somogyi, A., Van Zuilen, M. A., Medjoubi, K., et al. (2014). Evidence for arsenic metabolism and cycling by microorganisms 2.7 billion years ago. *Nature Geoscience*, *7*(11), 811–815. https://doi.org/10.1038/ngeo2276

Sforna, M. C., Daye, M., Philippot, P., Somogyi, A., van Zuilen, M. A., Medjoubi, K., et al. (2016). Patterns of metal distribution in hypersaline microbialites during early diagenesis: Implications for the fossil record. *Geobiology*, *15*(2), 259–279. https://doi.org/10.1111/gbi.12218

Shalev, E., Lyakhovsky, V., & Yechieli, Y. (2006). Salt dissolution and sinkhole formation along the Dead Sea shore. *Journal of Geophysical Research*, *111*(3), 1–12. https://doi.org/10.1029/2005JB004038

Sidle, W. C., Wotten, B., & Murphy, E. (2001). Provenance of geogenic arsenic in the Goose River basin, Maine, USA. *Environmental Geology*, *41*(1–2), 62–73. https://doi.org/10.1007/s002540100400

Singh, M., Pandey, S., Kumar, A., & Pandey, K. D. (2021). *Microbial biofilms for the remediation of contaminated water*. Microbe Mediated Remediation of Environmental Contaminants. INC. https://doi.org/10.1016/b978-0-12-821199-1.00021-3

Smith, P. G., Koch, I., Gordon, R. A., Mandoli, D. F., Chapman, B. D., & Reimer, K. J. (2005). X-ray absorption near-edge structure analysis of arsenic species for application to biological environmental simples. *Environmental Science and Technology*, *39*(1), 248–254. https://doi.org/10.1021/es049358b

Solé, V. A., Papillon, E., Cotte, M., Walter, P., & Susini, J. (2007). A multiplatform code for the analysis of energy-dispersive X-ray fluorescence spectra. *Spectrochimica Acta Part B: Atomic Spectroscopy*, *62*(1), 63–68. https://doi.org/10.1016/j.sab.2006.12.002

Sorrel, P., Jacq, K., Van Exem, A., Escarguel, G., Dietre, B., Debret, M., et al. (2021). Evidence for centennial-scale Mid-Holocene episodes of hypolimnetic anoxia in a high-altitude lake system from central Tian Shan (Kyrgyzstan). *Quaternary Science Reviews*, *252*, 106748. https://doi.org/10.1016/j.quascirev.2020.106748

Stüeken, E. E., Buick, R., Anderson, R. E., Baross, J. A., Planavsky, N. J., & Lyons, T. W. (2017). Environmental niches and metabolic diversity in Neoarchean lakes. *Geobiology*, *15*(6), 767–783. https://doi.org/10.1111/gbi.12251

Suosaari, E. P., Lascu, I., Oehlert, A. M., Parlanti, P., Mugnaioli, E., Gemmi, M., et al. (2022). Authigenic clays as precursors to carbonate precipitation in saline lakes of Salar de Llamara, Northern Chile. *Communications Earth and Environment*, *3*(1), 1–12. https://doi.org/10.1038/s43247-022-00658-5

Suosaari, E. P., Reid, R. P., Mercadier, C., Vitek, B. E., Oehlert, A. M., Stolz, J. F., et al. (2022). The microbial carbonate factory of Hamelin Pool, Shark Bay, Western Australia. *Scientific Reports*, *12*(1), 1–12. https://doi.org/10.1038/s41598-022-16651-z

Switzer, J., Allana, B., Bindi, B., Buzzelli, J., Stolz, J. F., & Oremland, R. S. (1998). Bacillus arsenicoselenatis, sp. nov., and Bacillus selenitireducens, sp. nov.: Two haloalkaliphiles from Mono Lake, California that respire oxyanions of selenium and arsenic. *Archives of Microbiology*, *171*(1), 19–30. https://doi.org/10.1007/s002030050673

Switzer, J., John, B., Aharon, F. S., & Oremland, R. S. (2001). Selenihalanaerobacter shriftii gen. nov., sp. nov., a halophilic anaerobe from Dead Sea sediments that respires selenate. *Archives of Microbiology*, *175*(3), 208–219. https://doi.org/10.1007/s002030100257

Team, R. C. (2013). R: A language and environment for statistical computing.

Thomas, C., Ebert, Y., Kiro, Y., Stein, M., & Ariztegui, D. (2016). Microbial sedimentary imprint on the deep Dead Sea sediment. *The Depositional Record*, *2*, 1–21. https://doi.org/10.1002/dep2.16

Thomas, C., Gedulter, N., Darvasi, Y., Bundeleva, I. A., Torfstein, A., Agnon, A., & Ariztegui, D. (2021). Arsenic enrichment and organomineralizations in microbial mats of the Dead Sea shores. In *Goldschmidt 2021 meeting abstracts*.

Thomas, C., & Ionescu, D. (2023). Combined genomic and imaging techniques show intense arsenic enrichment caused by detoxification in a microbial mat of the Dead Sea shore [Dataset]. OSF. https://doi.org/10.17605/OSF.IO/X5F8B

Thomas, C., Ionescu, D., Ariztegui, D., & DSDDP Scientific Team (2014). Archaeal populations in two distinct sedimentary facies of the subsurface of the Dead Sea. *Marine Genomics*, *17*, 53–62. https://doi.org/10.1016/j.margen.2014.09.001

Thomazo, C., Ader, M., & Philippot, P. (2011). Extreme 15N-enrichments in 2.72-Gyr-old sediments: Evidence for a turning point in the nitrogen cycle. *Geobiology*, *9*(2), 107–120. https://doi.org/10.1111/j.1472-4669.2011.00271.x

Visscher, P. T., Gallagher, K. L., Bouton, A., Farias, M. E., Kurth, D., Sancho-Tomás, M., et al. (2020). Modern arsenotrophic microbial mats provide an analogue for life in the anoxic Archean. *Communications Earth & Environment*, *1*(1), 1–10. https://doi.org/10.1038/s43247-020-00025-2

Wang, Y., & Qian, P. Y. (2009). Conservative fragments in bacterial 16S rRNA genes and primer design for 16S ribosomal DNA amplicons in metagenomic studies. *PLoS One*, *4*(10), e7401. https://doi.org/10.1371/journal.pone.0007401

Wang, Y., Wang, S., Xu, P., Liu, C., Liu, M., Wang, Y., et al. (2015). Review of arsenic speciation, toxicity and metabolism in microalgae. *Reviews in Environmental Science and Biotechnology*, *14*(3), 427–451. https://doi.org/10.1007/s11157-015-9371-9

Wong, H. L., Smith, D.-L., Visscher, P. T., & Burns, B. P. (2015). Niche differentiation of bacterial communities at a millimeter scale in Shark Bay microbial mats. *Scientific Reports*, *5*(1), 15607. https://doi.org/10.1038/srep15607

Wu, Y., Kukkadapu, R. K., Livi, K. J. T., Xu, W., Li, W., & Sparks, D. L. (2018). Iron and arsenic speciation during As(III) oxidation by manganese oxides in the presence of Fe(II): Molecular-level characterization using XAFS, Mössbauer, and TEM analysis. *ACS Earth and Space Chemistry*, *2*(3), 256–268. https://doi.org/10.1021/acsearthspacechem.7b00119

Xu, C., Zhou, T., Kuroda, M., & Rosen, B. P. (1998). Metalloid resistance mechanisms in prokaryotes. *Journal of Biochemistry*, *123*(1), 16–23. https://doi.org/10.1093/oxfordjournals.jbchem.a021904

Yan, P., Xia, J. S., Chen, Y. P., Liu, Z. P., Guo, J. S., Shen, Y., et al. (2017). Thermodynamics of binding interactions between extracellular polymeric substances and heavy metals by isothermal titration microcalorimetry. *Bioresource Technology*, *232*, 354–363. https://doi.org/10.1016/j.biortech.2017.02.067

Yang, H. C., & Rosen, B. P. (2016). New mechanisms of bacterial arsenic resistance. *Biomedical Journal*, *39*(1), 5–13. https://doi.org/10.1016/j.bj.2015.08.003

Yang, L., Nadeau, K., Meija, J., Grinberg, P., Pagliano, E., Ardini, F., et al. (2018). Inter-laboratory study for the certification of trace elements in seawater certified reference materials NASS-7 and CASS-6. *Analytical and Bioanalytical Chemistry*, *410*(18), 4469–4479. https://doi.org/10.1007/s00216-018-1102-y

Yechieli, Y., Abelson, M., Bein, A., Crouvi, O., & Shtivelman, V. (2006). Sinkhole "swarms" along the Dead Sea cost: Reflection of disturbance of lake and adjacent groundwater systems. *Bulletin of the Geological Society of America*, *118*(9–10), 1075–1087. https://doi.org/10.1130/B25880.1

Ying, S. C., Kocar, B. D., & Fendorf, S. (2012). Oxidation and competitive retention of arsenic between iron- and manganese oxides. *Geochimica et Cosmochimica Acta*, *96*, 294–303. https://doi.org/10.1016/j.gca.2012.07.013

Zander, P. D., Wienhues, G., & Grosjean, M. (2022). Scanning hyperspectral imaging for in situ biogeochemical analysis of lake sediment cores: Review of recent developments. *Journal of Imaging*, *8*(3), 58. https://doi.org/10.3390/jimaging8030058

Zargar, K., Hoeft, S., Oremland, R., & Saltikov, C. W. (2010). Identification of a novel arsenite oxidase gene, arxA, in the haloalkaliphilic, arsenite-oxidizing bacterium *Alkalilimnicola ehrlichii* strain MLHE-1. *Journal of Bacteriology*, *192*(14), 3755–3762. https://doi.org/10.1128/JB.00244-10

Zeyen, N., Benzerara, K., Li, J., Groleau, A., Balan, E., Robert, J. L., et al. (2015). Formation of low-T hydrated silicates in modern microbialites from Mexico and implications for microbial fossilization. *Frontiers in Earth Science*, *3*, 1–23. https://doi.org/10.3389/feart.2015.00064

Zhu, Y. G., Yoshinaga, M., Zhao, F. J., & Rosen, B. P. (2014). Earth abides arsenic biotransformations. *Annual Review of Earth and Planetary Sciences*, *42*(1), 443–467. https://doi.org/10.1146/annurev-earth-060313-054942

Zilberman, T., Gavrieli, I., Yechieli, Y., Gertman, I., & Katz, A. (2017). 1. Constraints on evaporation and dilution of terminal, hypersaline lakes under negative water balance: The Dead Sea, Israel. *Geochimica et Cosmochimica Acta*, *217*, 384–398. https://doi.org/10.1016/j.gca.2017.08.040